NUMERICAL ANALYSIS OF HELMHOLTZ RESONATORS UNDER LINEAR AND NONLINEAR EXCITATION IN SUBSONIC FLOW

Emerson Almeida Camargo

Dissertação de Mestrado
Ciências Mecânicas

UNIVERSIDADE DE BRASÍLIA

Faculdade de Tecnologia
Departamento de Engenharia Mecânica

UNIVERSIDADE DE BRASÍLIA
FACULDADE DE TECNOLOGIA
DEPARTAMENTO DE ENGENHARIA MECÂNICA

NUMERICAL ANALYSIS OF HELMHOLTZ RESONATORS UNDER LINEAR AND NONLINEAR EXCITATION IN SUBSONIC FLOW

Emerson Almeida Camargo

Orientador: Adriano Todorovic Fabro, Dr. (GDS/ENM/UnB)
Coorientador: Roberto F. Bobenrieth Miserda, Dr. (CAALab/ENM/UnB)

DISSERTAÇÃO DE MESTRADO

PUBLICAÇÃO: ENM.DM - XXX.XXX

BRASÍLIA/DF: 24 de março de 2021

UNIVERSIDADE DE BRASÍLIA
FACULDADE DE TECNOLOGIA
DEPARTAMENTO DE ENGENHARIA MECÂNICA

Numerical Analysis of Helmholtz Resonators Under Linear and Nonlinear Excitation in Subsonic Flow

Emerson Almeida Camargo

DISSERTAÇÃO DE MESTRADO SUBMETIDA AO DEPARTAMENTO DE ENGENHARIA MECÂNICA DA FACULDADE DE TECNOLOGIA DA UNIVERSIDADE DE BRASÍLIA COMO PARTE DOS REQUISITOS PARCIAIS PARA A OBTENÇÃO DO GRAU DE MESTRE EM CIÊNCIAS MECÂNICAS.

APROVADA POR:

Adriano Todorovic Fabro, Dr. (GDS/ENM/UnB)
(Orientador)

Roberto F. Bobenrieth Miserda, Dr. (CAALab/ENM/UnB)
(Coorientador)

Eder Lima de Albuquerque, Dr. (GFFM/ENM/UnB)
(Examinador Interno)

Yuri Dumaresq Sobral, Dr. (MAT/UnB)
(Examinador Externo)

BRASÍLIA/DF, 24 DE MARÇO DE 2021.

FICHA CATALOGRÁFICA

Camargo, E. A.
Numerical Analysis of Helmholtz Resonators Under Linear and Nonlinear Excitation in Subsonic Flow
[Distrito Federal] 2021.
xvii, 98p. (ENM/FT/UnB, Mestre, Ciências Mecânicas, 2021.
Dissertação de Mestrado - Universidade de Brasília.
Faculdade de Tecnologia.
Departamento de Engenharia Mecânica.
Palavras-chave:

1. Sound attenuation	2. Cylindrical liners
3. High subsonic flow	4. Immersed boundary method
I. ENM/FT/UnB	II. Título (série)

REFERÊNCIA BIBLIOGRÁFICA

Camargo, E. A.(2021). Numerical Analysis of Helmholtz Resonators Under Linear and Nonlinear Excitation in Subsonic Flow. Dissertação de Mestrado, Publicação ENM.DM - XXX.XXX, Departamento de Engenharia Mecânica, Universidade de Brasília, Brasília, Distrito Federal, xvii, 98p.

CESSÃO DE DIREITOS

NOME DO AUTOR: Emerson Almeida Camargo.

TÍTULO DA DISSERTAÇÃO DE MESTRADO: Numerical Analysis of Helmholtz Resonators Under Linear and Nonlinear Excitation in Subsonic Flow.

GRAU / ANO: MESTRE / 2021

Emerson Almeida Camargo

Aos meus pais, por todo apoio durante a caminhada.

Acknoledgements

This study was financed in part by the Coordenação de Aperfeiçoamento de Pessoal de Nível Superior – Brasil (CAPES) – Finance Code 001

Resumo

Numerical Analysis of Helmholtz Resonators Under Linear and Nonlinear Excitation in Subsonic Flow

Autor: Emerson Almeida Camargo

Orientador: Adriano Todorovic Fabro, Dr. (GDS/ENM/UnB)

Coorientador: Roberto F. Bobenrieth Miserda, Dr. (CAALab/ENM/UnB)

Programa de Pós Graduação em Ciências Mecânicas

Brasília, 24 de março de 2021

Situados nas entradas de dutos de *bypass*, os *liners* também podem ser usados na região de *interstage* de *turbofans* com alto *bypass* ou entre os rotores coaxiais utilizado em *eVTOL*s. Nestas regiões, o *liner* é submetido a uma componete tangencial de velocidade associada a fortes efeitos não lineares, que podem diminuir significativamente seu desempenho. Neste trabalho, uma abordagem numérica é proposta para investigar a interação acústica de um *liner* em um duto com fontes de ruído não lineares quando submetidos a um escoamento subsônico. As simulações foram conduzidas utilizando-se as equações de Euler para modelar um escoamento invíscido, transiente e compressível. O método de fronteira imersa é utilizado para impor as condições de contorno associadas à geometria de uma matriz de ressonadores e um canal com simetria plana. Os principais resultados incluem: um canal simples com escoamento e fonte de pressão; um canal com ressonadores e escoamento; e também um canal com ressonadores, escoamento e fonte de pressão. Simulações do canal simples mostram o potencial da abordagem numérica proposta para a geração de ondas N com uma frequência e nível de pressão sonora prescritos. Além disso, uma configuração que inclui o duto com ressonadores e fluxo mostra o ruído autoinduzido do *liner* com características de onda N, devido à interação do fluxo com os ressonadores. No terceiro caso, o ruído autoinduzido do *liner* interage com uma fonte distribuída de ruído harmônico de alta amplitude. As respostas no domínio do tempo e da frequência são usadas para discutir o desempenho acústico dessa configuração. Eles mostram que para o primeiro harmônico da fonte não linear, a redução do ruído tonal é de 5 dB, assim

como 20 dB para o segundo harmônico, 23,5 dB para o terceiro e 15,5 dB para o quarto. Esses resultados sugerem a ação de uma interferência destrutiva invíscida entre as ondas N geradas pelos revestimentos cilíndricos e as fontes não lineares sob um fluxo alto subsônico em um duto plano.

Palavras-chaves: Sound attenuation; Cylindrical liners; High subsonic flow; Immersed boundary method.

Abstract

NUMERICAL ANALYSIS OF HELMHOLTZ RESONATORS UNDER LINEAR AND NONLINEAR EXCITATION IN SUBSONIC FLOW

Author: Emerson Almeida Camargo

Supervisor: Adriano Todorovic Fabro, Dr. (GDS/ENM/UnB)

Co-Supervisor: Roberto F. Bobenrieth Miserda, Dr. (CAALab/ENM/UnB)

Master in Mechanical Sciences

Brasília, 2021

Placed at intakes and bypass ducts, liners can also be used in the interstage region of very high bypass ratio turbofans or between ducted coaxial rotors for eVTOL applications. In this region, the liner is subjected to a swirl component associated with strong nonlinear effects, which can significantly decrease its acoustic performance. In this work, a numerical approach is proposed to investigate the acoustic interaction of a lined array of resonators whit nonlinear noise sources when subjected to high subsonic flow. The simulations were carried using the Euler equations to model the unsteady and compressible inviscid flow. An immersed boundary method is used to impose the boundary conditions associated with the geometry of the arrays of cylindrical liners and a channel with plane symmetry. Main results include a simple channel with flow and source, a lined channel with flow, and also a lined channel with flow and source. Simulations of the simple channel show the potential of the proposed numerical approach for generating N-waves with a prescribed frequency and sound pressure level. Moreover, a numerical setup that includes a lined channel configuration with flow shows the resulting liner self-noise with N-wave characteristics, due to the interaction of the flow with the resonators. In the third case, liner self-noise interacts with a high- amplitude, harmonic, and distributed noise source. Time and frequency domain responses are used to discuss the acoustic performance of this configuration. They show that for the first harmonic of the nonlinear source, the tone noise reduction is 5dB, as well as 20dB for the second harmonic, 23.5dB for the third one, and 15.5dB for the fourth. These results suggest the action of an inviscid destructive

interference between the N-waves generated by the cylindrical liners and the nonlinear sources under a high subsonic flow in a channel.

Key-words: Sound attenuation, cylindrical liners, high subsonic flow, immersed boundary method

Summary

1 INTRODUCTION 1
1.1 Aircraft Certification 1
1.2 Aircraft Noise Sources 4
1.3 Acoustic Liner 4
1.4 Objectives 7
1.5 Methodology 8
1.6 Dissertation overview 8

2 NUMERICAL METHODOLOGY 9
2.1 Governing Equations 9
2.2 Finite-Volume Discretization 10
2.3 Interpolation Scheme 13
2.4 Artificial Dissipation 14
2.5 Time Integration 15
2.6 Immersed Boundary Method 15
2.7 Computational Implementation 17

3 NUMERICAL RESULTS 19
3.1 Single resonator 19
3.1.1 Case 1 19
3.1.2 Case 2 21
3.1.3 Case 3 22
3.1.4 Case 4 24
3.1.5 Case 5 25
3.1.6 Case 6 26
3.1.7 Case 7 28
3.1.8 Case 8 29
3.1.9 Case 9 30
3.1.10 Case 10 31
3.1.11 Case 11 32

3.1.12 Case 12 and 13 33
3.2 Liner configuration 36
3.2.1 Flow and source 37
3.2.2 Flow and cylindrical liners 39
3.2.3 Flow, source, and cylindrical liners 42
3.2.4 Frequency domain analysis 42

4 CONCLUSIONS 47
4.1 Suggestions for further work 47

BIBLIOGRAPHY 48

List of Figures

Figure 1.1 – Flight profiles for aircraft certification (BÖTTCHER, 2004). 2
Figure 1.2 – Measurement point (BÖTTCHER, 2004). 3
Figure 1.3 – Typical liner configuration with a rigid backplate, a honeycomb structure and a perforated facesheet 5
Figure 1.4 – Sketch of a resonator with main geometrical parameters (SPILLERE, 2017) 6
Figure 2.1 – Schematic grid: regular region with 8x4 control volumes and 4 stretched volumes for each direction. 12
Figure 2.2 – Representation of VAT's Cartesian mesh 12
Figure 2.3 – Illustration of immersed boundary method. 16
Figure 3.1 – Numerical setup for case 1. 20
Figure 3.2 – Visualization with β_T for case 1. 20
Figure 3.3 – Numerical setup for case 2. 21
Figure 3.4 – Visualization with β_T for case 2. 22
Figure 3.5 – Numerical setup for case 3. 23
Figure 3.6 – Visualization with β_T for case 3. 23
Figure 3.7 – Numerical setup for case 4. 24
Figure 3.8 – Visualization with β_T for case 4. 25
Figure 3.9 – Numerical setup for case 5. 25
Figure 3.10–Visualization with β_T for case 5. 26
Figure 3.11–Numerical setup for case 6. 27
Figure 3.12–Visualization with β_T for case 6. 27
Figure 3.13–Numerical setup for case 7. 28
Figure 3.14–Visualization with β_T for case 7. 28
Figure 3.15–Numerical setup for case 8. 29
Figure 3.16–Visualization with β_T for case 8. 30
Figure 3.17–Numerical setup for case 9. 31
Figure 3.18–Visualization with β_T for case 9. 31
Figure 3.19–Numerical setup for case 10. 32
Figure 3.20–Visualization with β_T for case 10. 32

Figure 3.21–Numerical setup for case 11. 33
Figure 3.22–Visualization with β_T for case 11. 33
Figure 3.23–Numerical setup for case 12. 34
Figure 3.24–Visualization with β_T for case 12. 34
Figure 3.25–Numerical setup for case 13. 35
Figure 3.26–Visualization with β_T for case 13. 35
Figure 3.27–Comparisson between sprectra for circular and square liner. 36
Figure 3.28–Geometry the plane channel, the arrays of liners and the distributed source. 38
Figure 3.29–Dimensional parameters for the geometry of the cylindrical liners shown over the left end of the lower array. 38
Figure 3.30–Resolution of the volumetric (Cartesian) and surface grids shown at the throat of the cylindrical liner. 39
Figure 3.31–Visualization of the aeroacoustic flowfield for the flow and source case. 40
Figure 3.32–Pressure signal at the inlet of the channel for the flow and source case. 40
Figure 3.33–Visualization of the aeroacoustic flowfield for the flow and cylindrical liners case. 41
Figure 3.34–Pressure signal at the inlet of the channel for the flow and cylindrical liners case. 41
Figure 3.35–Visualization of the aeroacoustic flowfield for the flow, source and cylindrical liners. 43
Figure 3.36–Pressure signal at the inlet of the channel for the flow, source and cylindrical liners. 43
Figure 3.37–Effect of the acoustic treatment over the nonlinear waves. 44
Figure 3.38–Sound pressure level spectrum at the inlet of the channel for the flow and source case. 45
Figure 3.39–Sound pressure level spectrum at the inlet of the channel for the flow and cylindrical liners case. 45
Figure 3.40–Sound pressure level spectrum at the inlet of the channel for the flow, source, and cylindrical liners case. 46
Figure 3.41–Effect of the acoustic treatment using cylindrical liners on the sound pressure level at the inlet of the channel. 46

List of abbreviations and acronyms

$ICAO$	International Civil Aviation Organization
FAA	Federal Aviation Administration
$NPRM$	Notice of Proposed Rulemaking
FAR	Federal Aviation Regulations
PNL	Perceived Noise Level
$EPNL$	Effective Perceived Noise Level
SPL	Sound Pressure Level
MPT	Multiple Pure Tone
VAT	Virtual Aeroacoustic Tunnel

List of symbols

c_p	Heat capacity at constant pressure $[J/K]$
c_v	Heat capacity at constant volume $[J/K]$
e	Internal energy
e_T	Total energy
$\mathbf{E}$	x-component flux vector
$\mathbf{U}$	y-component flux vector
f_x	x-component field force
f_y	y-component field force
$\mathbf{f}$	Field Force
$\hat{\imath}$	x-direction Unitary Vector
$\hat{\jmath}$	y-direction Unitary Vector
$\mathbf{n}$	Normal vector
p	Pressure
R	Gas constant $[J/kg.K]$
$\mathbf{R}$	Vector of field forces
$\overline{\mathbf{R}}$	Volumetric mean of $\mathbf{R}$
S	Surface area $[m^2]$
$\mathbf{S}$	Vector surface area
t	Time $[s]$
T	Temperature $[K]$
u	x-component speed $[m/s]$

$\mathbf{U}$	Vector of conservative variables
$\overline{\mathbf{U}}$	Volumetric mean of $\mathbf{U}$
v	y-component speed $[m/s]$
V	Volume
$\mathbf{V}$	Velocity $[m/s]$
β_T	Visualization variable
γ	Heat capacity ratio
ρ	Density $[kg/m^3]$
Π	Flux tensor

1 Introduction

Air transportation plays an important role in the modern world. Air travel has crossed international frontiers, brought nations close together, boosted world markets, and provided many people the pleasure of visiting the numerous faraway places that are now readily accessible in a short traveling time. Modern aviation started around the 1950s with Havilland Comet, the earliest commercial aircraft powered by a jet engine. The noise created by early jet engines warned the industry about a problem, and the reaction of communities was sufficient to confirm a need for research about the noise of gas turbine aeroengines. Then, aeroengines evolved to the modern turbofans, airports have expanded, many new others have appeared and "noise-impacted zones" have spread (SMITH, 1989).

1.1 Aircraft Certification

Aiming to ensure minimal noise impact to the environment, certification of aircraft includes directives for noise. In 1968, International Civil Aviation Organization (ICAO) Assembly adopted a resolution that conceded the seriousness of noise and instructed the ICAO Council to establish international specifications and guidance material to control aircraft noise, and in 1971, Annex 16 was adopted (ICAO, 2012). This annex has two volumes and deals with the protection of the environment, with volume I dealing with aircraft noise. The Federal Aviation Administration (FAA) announced in 1969 via NPRM 69-1 practical structure for a noise certification scheme and in 1971, after analysis of public and industry response to NPRM 69-1, a noise certification scheme emerged in the form of FAR Part 36 (SMITH, 1989).

The human hearing system responds to a wide range of frequencies and sound pressure levels, are most disturbed by frequencies between 2 kHz and 4 kHz, and do not responds uniformly to sounds of the same intensity generated at different frequencies, then, the certification scheme needed a metric that varies either intensity or frequency to express a human response to loudness and annoyance (or perceived noisiness) of aircraft noise (DEPITRE, 2006). The basic element for noise certification criteria is known as EPNL (Effective Perceived Noise Level), in units of EPNdB. This metric is a measure of subjective effects of airplane noise on human beings, and is calculated based on instantaneous PNL (Perceived Noise Level) corrected for spectral irregularities and needs the measuring of

three basic physical properties of sound: level, frequency distribution, and time variation (CFR. . . , 1969).

The process of aircraft certification described in Annex 16 Volume I and FAR Part 36, is based on noise measurements evaluated during the flight under certain conditions. Figure 1.1 presents the flight profiles that aircraft must follow for Lateral, Flyover, and approach reference measurements in Figure 1.2.

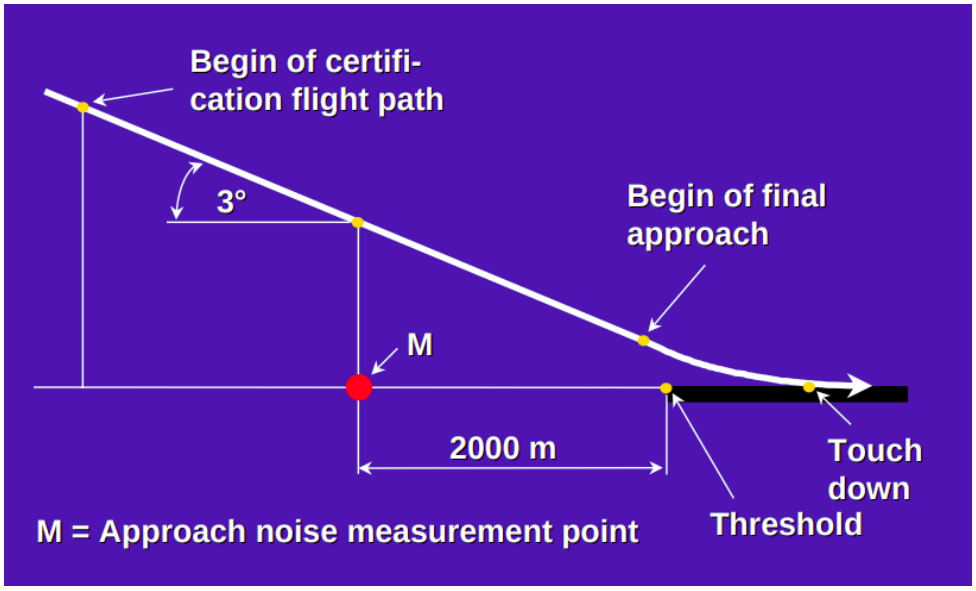

(a) Approach reference procedure.

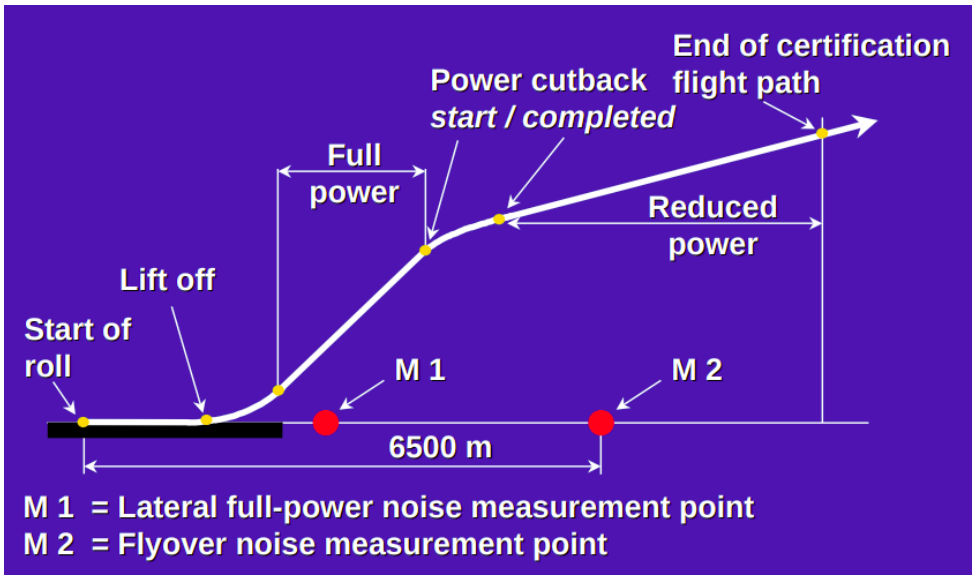

(b) Take-off reference procedure.

Figure 1.1 – Flight profiles for aircraft certification (BÖTTCHER, 2004).

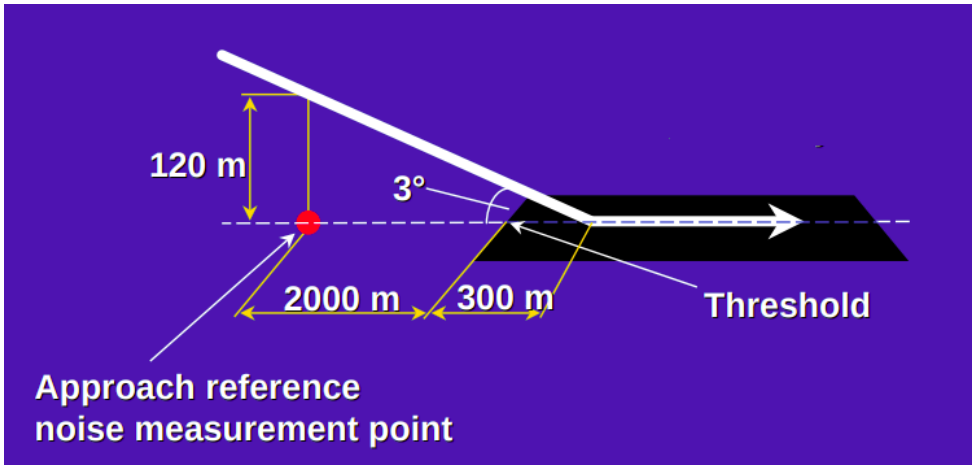

(a) Approach reference noise measurement point.

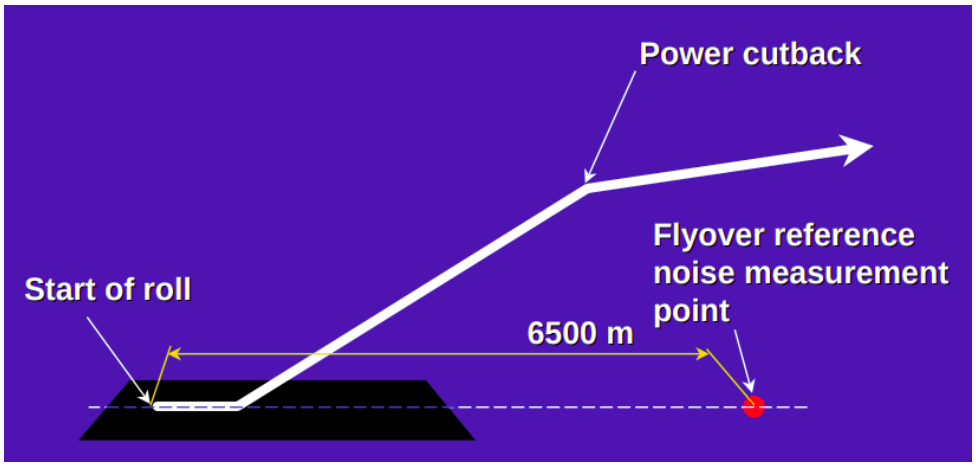

(b) Flyover reference noise measurement point.

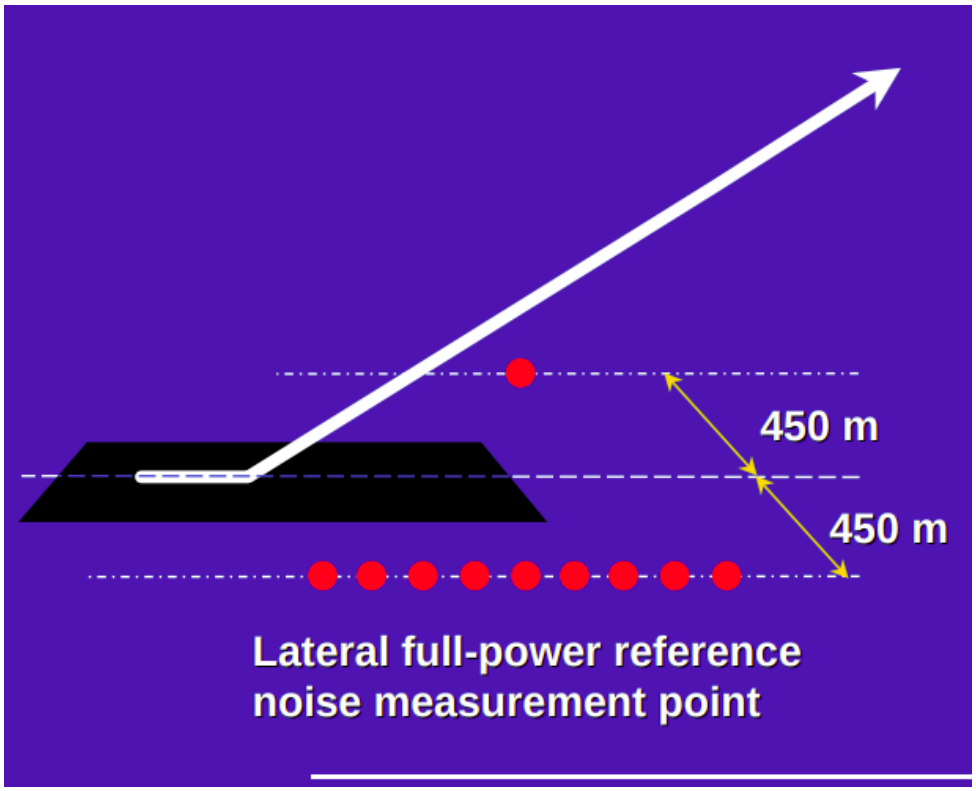

(c) Lateral reference noise measurement point.

Figure 1.2 – Measurement point (BÖTTCHER, 2004).

1.2 Aircraft Noise Sources

In order to reduce aircraft generated noise, the first step is to identify the noise sources. The airframe itself is a source, with air flowing over different structures, such as landing gears, wheel bays, high-lift devices (flaps and slats), wings, etc. Due to the fact of different sizes of the structures, the noise generated by the airframe has a broadband characteristic. Another main noise source is the propulsion systems, which is the major source of noise (SMITH, 1989). The most used propulsion system for commercial aircraft is the turbofan, which generated noise has mixed broadband and tonal noise spectrum, where the tonal peaks are mainly associated with the fan rotor-stator interaction. The recent trend towards very-high bypass ratio turbofans emphasizes the importance of this noise source.

1.3 Acoustic Liner

Considering the requirements for lowering the aircraft noise, it is necessary to develop means of noise suppression. The acoustic liner is one of the most effective means to suppress fan noise in turbofans (TAM; JU; WALKER, 2008). They have become standard for the aircraft industry in control of excessive turbofan engine inlet/exhaust noise (HERSH; WALKER; CELANO, 2003).

The tone component of this noise is a set of cut-on azimuthal and radial duct modes (SUTLIFF, 2005), whereas the former is essentially a set of Mach waves moving with a supersonic azimuthal speed (MISERDA; PIMENTA; ROCHA, 2020) and a characteristic N-wave format, with a linear decay of pressure between two peaks. A sequence of these waves creates the sawtooth wave format and for a turbofan operating at off-design conditions, like takeoff, a slight disruption of that pattern due to slight differences in the geometry of the fan blades, results in an upstream cascading coalescence of N-waves that result in Multiple Pure Tone (MPT) noise generation (PIMENTA; MISERDA, 2019).

N-waves are fundamental elements of nonlinear acoustics (ENFLO; HEDBERG, 2002) since for any plane wave propagating in a duct, the peaks will propagate faster than the valleys due to the difference in the local speed of sound. Eventually, the faster trailing peak will catch up with the slower leading valley and, since the peak cannot overtake over the valley, a sharp discontinuity is formed and, depending on the intensity levels, results in a series of Mach waves, similar to tone noise due to rotor-stator interaction, or shock waves, similar to MPT noise. This phenomenon does not exist in linear acoustics since the speed of sound is assumed constant in the whole propagation domain.

Figure 1.3 presents a usual scheme of a liner: a rigid backplate, a honeycomb structure, and a perforated faceshield. In this way, the liner can be seen as an array of Helmholtz resonators. A large number of research papers in the last decades are dedicated

to understanding the dissipation mechanism of these resonators. They have shown that different excitation conditions lead to different responses of resonators, such as grazing-flow, high pressures, high velocities, high temperatures, etc.

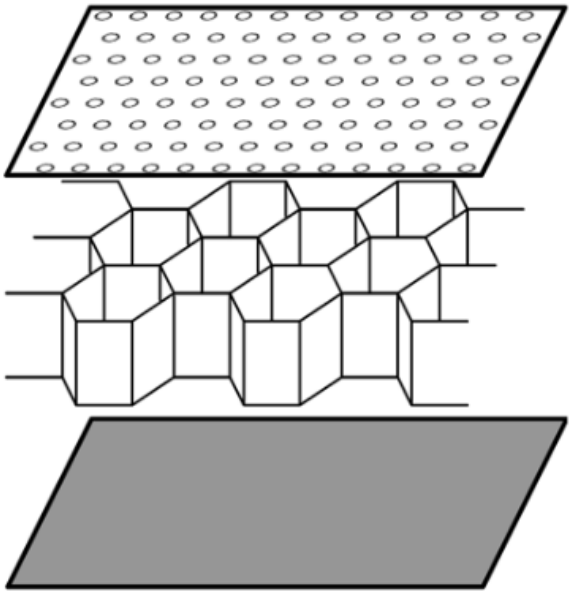

Figure 1.3 – Typical liner configuration with a rigid backplate, a honeycomb structure and a perforated facesheet

Current trends for the next generation of turbofans engines are towards a higher bypass ratio, aiming for better efficiency and lower noise along with increased distances between the fan and the outlet guide vanes. These trends mean, however, higher nacelle diameters with increased drag, thus introducing the need for a reduction in the length of the nacelle. Commonly placed at intakes and bypass ducts, liners can also be used in the interstage region. However, in this region, the liner is subjected to a swirl component associated with strong nonlinear effects, which can significantly decrease its acoustic performance. The consequences of this scenario are the overall reduction of lined surface areas as well as the increase in the relative importance of the interstage liner.

Acoustic liners are used in internal walls of aero-engines for noise treatment. In general, they have fixed geometry and act as passive acoustic treatment. According to Motsinger and Kraft (1991) the panel design and the associated suppression depend on the noise source characteristics, and the design of the liner must match as closely as possible the impedance for each frequency band of concern. Impedance is the important design parameter and is expressed as a complex number, with a real part, the resistance, and the imaginary part, the reactance.

There ate different types of liners, with different frequencies of suppression. Figure 1.3, shows a single degree of freedom (SDOF) liner, with a perforated facesheet, a rigid backplate, and a honeycomb. Adding a second layer of honeycomb with a porous septum results in a two-degree of freedom (2DOF) liner. Instead of the honeycomb, it is possible

to use a fibrous material to build a bulk absorber. The SDOF is the most searched and is the focus of this work. Figure 1.4 show the main parameters for constructions of a SDOF: facesheet thickness (τ), perforate diameter (d) and cavity depth (l).

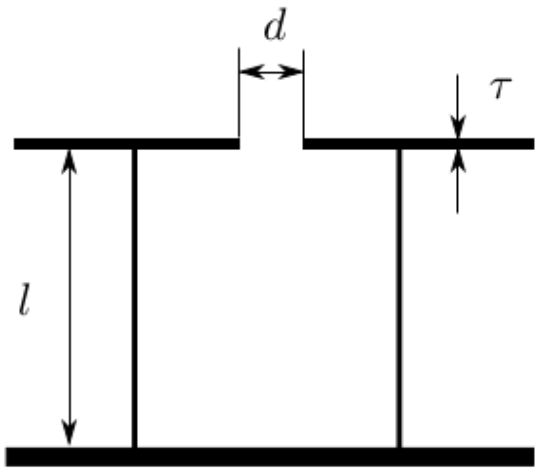

Figure 1.4 – Sketch of a resonator with main geometrical parameters (SPILLERE, 2017)

Since acoustic liner became standard in noise control, a large research effort on understanding its behavior has been made. Many papers were published studying impedance of orifices, perforated plates, and mediums or Helmholtz resonator arrays. In the different aero-engines and different parts, liners are subjected to different conditions. These conditions, such as high speed, high temperature, grazing flow, bias flow, etc. were broadly studied.

Due to the complexity, methods for impedance eduction are empirical or semi-empirical. Melling (1973) carried out studies of acoustic impedance of a range of perforates at medium and high sound pressure level and recognized the dependence of the liner's behavior with the incident sound pressure level (SPL). In practice, the change becomes apparent at 130 dB, with an increase of resistance together with a decrease in reactance. Dean (1974) worked in a novel method for impedance measurement for local application with the usage of two microphones, the first one placed at the facesheet and the other in the backplate. The two-microphone method is broadly used in the following works.

Hughes and Dowling (1990), Dowling and Hughes (1992) considered the liner placed in the afterburner section of jet engines and presented a study of perforated screen backed with rigid plate with bias flow. The bias flow is a mean flow through the hole, and the interaction between incident sound waves and the mean flow converts acoustic energy into unsteady vortical motion. Jing and Sun (1999) also investigates perforated liners with bias flow, and experimental results showed that the presence of bias flow markedly increases both the absorption coefficient and effective bandwidth. Eldredge and Dowling (2003) developed a one-dimensional model that considers that the liner converts acoustical energy

into flow energy with vortex shedding.

Malmary et al. (2001) evaluate measurements of acoustic impedance under grazing flow, using the two-microphone method. Grazing flow is a flow parallel to the facesheet, this condition is found in the inlet of turbofans. In these conditions, the liner experiences velocities up to Mach 0.7 and sound waves with a frequency between 800 Hz and 8000 Hz and levels up to 160 dB. Jing et al. (2001) developed a model to study the effect of grazing flow in the impedance of an orifice.

Liner behavior is different under linear and nonlinear conditions. Hersh, Walker and Celano (2003) derived a nonlinear impedance model using a described behavior of inlet/exhaust oscillatory jets in neck resonators for high sound pressure levels.

Advances in computation made the numerical investigation of this phenomenon possible. Many works investigate numerical methodologies for simulations of acoustic liners. Another branch in the numerical investigation is the derivation of time-domain impedance boundary conditions, aiming for application in simulations without the direct modeling of acoustic liners.

Tam and Auriault (1996) derived a time-domain impedance boundary condition for numerical simulations. Such boundary condition has not been considered before. Özyörük, Long and Jones (1998) simulated an impedance tube to validate a proposed time-domain time condition. Tam and Kurbatskii (2000), Tam et al. (2001) used direct numerical simulation to investigate the fluid dynamics around the neck of a resonator with an incident wave and described mechanisms for attenuation in low and high sound intensity. They describe an oscillatory boundary layer at a low sound intensity and vortex shedding at a high sound intensity and showed that the vortex shedding is efficient energy dissipation. Tam et al. (2005) and Tam, Ju and Walker (2008) carried out computational and experimental studies for a slit resonator with an incident wave. Zhang and Bodony (2011) developed an impedance eduction technique solving compressible Navier-Stokes. Tam et al. (2014) carried numerical simulation and experimental studies with an array of eight slit resonators under grazing flow.

1.4 Objectives

In this work, a numerical approach is proposed to investigate the acoustic interaction of a lined array of resonators when subject to high subsonic flow and high amplitude pressure sources. Boundary conditions associated with the array of cylindrical liners are imposed by an immersed boundary method.

1.5 Methodology

Three test cases are investigated with increasing complexity. Firstly, a simple channel with a flow and a nonlinear source, then a lined channel with a subsonic flow, and finally, a lined channel with a flow and a nonlinear source. Time and frequency domain results are obtained from measurement probes along the channel in addition to the visualization of the aeroacoustic field throughout the computational domain. It is shown that the proposed approach can effectively simulate nonlinear responses due to the source excitation and the interaction with the liners.

1.6 Dissertation overview

This dissertation is organized as follows. Chapter 1 presents an introduction with the paper aim, methodology, and a summary of the results. Chapter 2 introduces the numerical method, based on the Euler equations and immersed boundary method for modeling the inviscid, unsteady and compressible flow. Subsequently, Chapter 3 presents the numerical setup and the numerical cases for the proposed investigation as well as the numerical results for the proposed cases along with a discussion. Finally, Chapter 4 gives the concluding remarks and suggestions for further work.

2 Numerical Methodology

This chapter presents the numerical methodology already implemented in the Virtual Aeroacoustic Tunnel (VAT) code, developed by the Computational Aeroacoustics Laboratory (CAALab), as well as the necessary modifications implemented in the source code by the author in other to achieve the objectives of this work.

2.1 Governing Equations

In order to simulate a compressible inviscid transient flow, the Euler's equations are used. These are the continuity, momentum and energy equations given by

$$\frac{\partial \rho}{\partial t} + \nabla \cdot (\rho \mathbf{V}) = 0, \tag{2.1}$$

$$\frac{\partial (\rho \mathbf{V})}{\partial t} + \nabla \cdot (\rho \mathbf{V} \otimes \mathbf{V}) = -\nabla p + \mathbf{f}, \tag{2.2}$$

$$\frac{\partial (\rho e_T)}{\partial t} + \nabla \cdot (\rho e_T \mathbf{V}) = -\nabla \cdot (p \mathbf{V}) + \mathbf{f} \cdot \mathbf{V}, \tag{2.3}$$

where ρ is density, u is the x-component velocity, v is the y-component velocity, $\mathbf{V} = u\hat{\imath} + v\hat{\jmath}$ is the velocity (a two-dimensional version of the methodology was used in this work), p is the pressure, f_x is the x-component field force, f_y is the y-component field force, $\mathbf{f} = f_x\hat{\imath} + f_y\hat{\jmath}$ is the field force, t is time, and e_T is the total energy, defined as

$$e_T = e + \frac{|\mathbf{V}|^2}{2} = e + \frac{u^2 + v^2}{2}, \tag{2.4}$$

There are five unknowns in this system of equations, namely, density (ρ), x-component velocity (u), y-component velocity (v), pressure (p) e internal energy (e). In order to make it consistent, two constitutive relations can be added: equation for the internal energy of calorically perfect gas

$$e = c_v T, \tag{2.5}$$

and equation of state for ideal gases

$$p = \rho RT = \rho e(\gamma - 1), \tag{2.6}$$

where $\gamma = c_p/c_v$ is the heat capacity ratio.

Equations 2.1 to 2.3 can be written in more compact vectorial notation, that will be useful in the discretization of a two-dimensional domain as

$$\frac{\partial \mathbf{U}}{\partial t} + \frac{\partial \mathbf{E}}{\partial x} + \frac{\partial \mathbf{F}}{\partial y} = \mathbf{R} \tag{2.7}$$

where

$$\mathbf{U} = \begin{pmatrix} \rho \\ \rho u \\ \rho v \\ \rho e_T \end{pmatrix}, \mathbf{E} = \begin{pmatrix} \rho u \\ \rho uu + p \\ \rho uv \\ (\rho e_T + p)u \end{pmatrix}, \mathbf{F} = \begin{pmatrix} \rho v \\ \rho vu \\ \rho vv + p \\ (\rho e_T + p)v \end{pmatrix}, \mathbf{R} = \begin{pmatrix} 0 \\ f_x \\ f_y \\ f_x u + f_y v \end{pmatrix}. \tag{2.8}$$

$\mathbf{U}$ is the vector of conservative variables which elements are the intensive properties, per unit volume, related to mass, momentum, and energy. $\mathbf{E}$ and $\mathbf{F}$ are the flux vectors, and $\mathbf{R}$ is the vector of field forces and shows how each variable varies according to a field force. This field force is present in a non-inertial frame of reference, that is, for a reference that follows the geometry in a flow (and accelerates with it), the acceleration process is described by vector $\mathbf{R}$. The pseudo-forces are associated with the components of the free flow velocity, u_∞ and v_∞ by the relations $f_x = \rho(u_\infty/t_a)$ and $f_y = \rho(v_\infty/t_a)$, where t_a is the acceleration time. After the acceleration time, the Euler equation recovers the form used in an inertial frame of reference, where $\mathbf{R} = 0$

2.2 Finite-Volume Discretization

Defining the flux tensor

$$\Pi = \mathbf{E} \otimes \mathbf{i} + \mathbf{F} \otimes \mathbf{j} \tag{2.9}$$

equation 2.7 can be rewritten as

$$\frac{\partial \mathbf{U}}{\partial t} + \nabla \cdot \Pi = \mathbf{R}. \tag{2.10}$$

Integrating equation 2.10 over a control volume, V, and dividing by its volume yields

$$\frac{\partial}{\partial t}\left(\frac{1}{V}\int_V \mathbf{U} dV\right) = -\frac{1}{V}\int_V (\nabla \cdot \Pi) dV + \left(\frac{1}{V}\int_V \mathbf{R} dV\right). \tag{2.11}$$

Defining $\overline{\mathbf{U}}$ and $\overline{\mathbf{R}}$ as the volumetric mean of the properties

$$\overline{\mathbf{U}} = \frac{1}{V}\int_V \mathbf{U} dV, \qquad \overline{\mathbf{R}} = \frac{1}{V}\int_V \mathbf{R} dV \tag{2.12}$$

and applying the divergence theorem for the first term of right-hand side

$$\int_V (\nabla \cdot \Pi) dV = \int_S (\Pi \cdot \mathbf{n}) dS, \tag{2.13}$$

equation 2.11 can be rewritten as

$$\frac{\partial \overline{\mathbf{U}}}{\partial t} = -\frac{1}{V} \int_S (\Pi \cdot \mathbf{n}) dS + \overline{\mathbf{R}}, \tag{2.14}$$

where S is the area and $\mathbf{n}$ is the outward normal vector of the surface S.

The finite volume discretization domain is composed of two different regions: the regular region and the stretched region. The regular region is discretized by square control volumes of equal size and is the region of interest in simulations, where the geometry is placed. The stretched region surrounds the regular one. Each volume in this region has an area slightly bigger than the previous one and this growth happens from de center (regular region) and goes into the domain edge. The aiming of the stretched region is to serve as natural boundary conditions.

Figure 2.1 illustrates a small, schematic, domain. In the center, the brighter group of volumes surrounded by the box with ticker lines is the regular region. In this schematic domain, it has 8x4 control volumes. The region outside the box is the stretched region. Here, each volume length is higher than the previous by a multiplier factor. This scheme has four control volumes in each direction and the factor is 1.3, that is, each volume is 30% (thirty percent) larger than the previous one. This means that the stretched region grows exponentially in all directions, as it occurs, a small and convenient number of control volumes gives enormous inertia to the flow and makes the boundary of the domain far enough so that they are not reached by fluctuations in the simulation duration.

Figures 2.2 illustrates a generic control volume (i, j) in the VAT's Cartesian mesh. Figure 2.2a shows the control volume painted in blue, the surfaces delimiting the volume in red, and the normals related to each surface in green.

For the control volume (i, j), with this geometry, equation 2.14 can be written as

$$\frac{\Delta \overline{\mathbf{U}}_{i,j}}{\Delta t} = -\frac{1}{V_{i,j}} \left[(\Pi \cdot \mathbf{S})_{i+\frac{1}{2}} + (\Pi \cdot \mathbf{S})_{i-\frac{1}{2}} + (\Pi \cdot \mathbf{S})_{j+\frac{1}{2}} + (\Pi \cdot \mathbf{S})_{j-\frac{1}{2}} \right] + \overline{\mathbf{R}}_{i,j}. \tag{2.15}$$

From Equation 2.14 to 2.15, the time derivative was discretized and the integral term of was replaced by a sum of each area $\mathbf{S}$. The sub-index $i + \frac{1}{2}$ means the surface dividing (i, j) and $(i + 1, j)$, then $(\Pi \cdot \mathbf{S})_{i+\frac{1}{2}}$, $(\Pi \cdot \mathbf{S})_{i-\frac{1}{2}}$ $(\Pi \cdot \mathbf{S})_{j+\frac{1}{2}}$ $(\Pi \cdot \mathbf{S})_{j-\frac{1}{2}}$ indicates, respectively, right, left, top and bottom flux of tensor Π in volume (i, j). Equation 2.15 tells that the change of vector $\overline{U}$ after a time step Δt is related to two different sources, namely the flux of the properties through the surface $(\Pi \cdot \mathbf{S})$ and the body force acting over the control volume $(\overline{\mathbf{R}})$. It can be rewritten as

$$\Delta \overline{\mathbf{U}}_{i,j}, = -\mathcal{F}_{i,j} + \mathcal{R}_{i,j}, \tag{2.16}$$

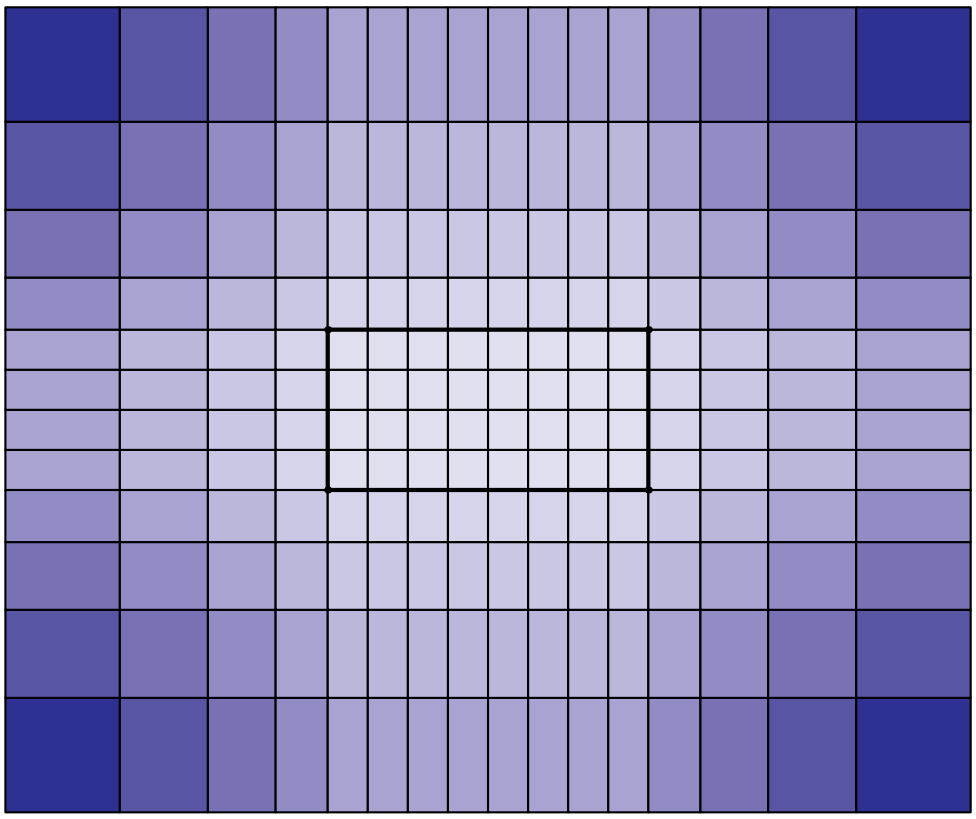

Figure 2.1 – Schematic grid: regular region with 8x4 control volumes and 4 stretched volumes for each direction.

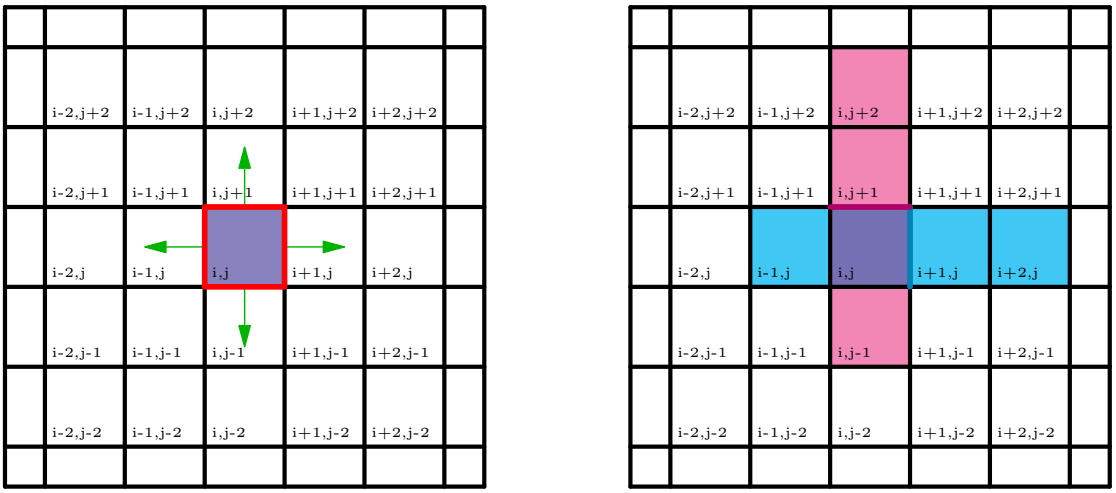

(a) Control volume (light blue) with surfaces (red) and normals (green)

(b) Example of stencil used for surface interpolation (blue for right surface and red for top surface)

Figure 2.2 – Representation of VAT's Cartesian mesh

where

$$\mathcal{F}_{i,j} = \frac{\Delta t}{V_{i,j}} \left[(\Pi \cdot \mathbf{S})_{i+\frac{1}{2}} + (\Pi \cdot \mathbf{S})_{i-\frac{1}{2}} + (\Pi \cdot \mathbf{S})_{j+\frac{1}{2}} + (\Pi \cdot \mathbf{S})_{j-\frac{1}{2}} \right], \qquad \textit{and} \tag{2.17}$$

$$\mathcal{R}_{i,j} = \Delta t \cdot \overline{\mathbf{R}}_{i,j}. \tag{2.18}$$

2.3 Interpolation Scheme

In order to calculate $\mathcal{F}_{i,j}$, the flux $(\Pi \cdot \mathbf{S})$ must be evaluated for each surface. For the Cartesian mesh presented in section 2.2, figure 2.2a, the surface vector $\mathbf{S} = s_x\mathbf{i} + s_y\mathbf{j}$ has only one component, in other words, either s_x or s_y are zero. Then, the area of surfaces can be written as

$$S_{i+\frac{1}{2}} = \quad s_x\mathbf{i} \tag{2.19}$$

$$S_{i-\frac{1}{2}} = - \; s_x\mathbf{i} \tag{2.20}$$

$$S_{j+\frac{1}{2}} = \quad s_y\mathbf{j} \tag{2.21}$$

$$S_{j-\frac{1}{2}} = - \; s_y\mathbf{j} \tag{2.22}$$

and the fluxes becomes

$$(\Pi \cdot \mathbf{S})_{i+\frac{1}{2}} = (\Pi \cdot s_x\mathbf{i}) = \begin{bmatrix} \rho_{i+\frac{1}{2}} u_{i+\frac{1}{2}} s_x \\ (\rho u)_{i+\frac{1}{2}} u_{i+\frac{1}{2}} s_x + p_{i+\frac{1}{2}} s_x \\ (\rho v)_{i+\frac{1}{2}} u_{i+\frac{1}{2}} s_x \\ (\rho e_T)_{i+\frac{1}{2}} u_{i+\frac{1}{2}} s_x + p_{i+\frac{1}{2}} u_{i+\frac{1}{2}} s_x \end{bmatrix} \tag{2.23}$$

$$(\Pi \cdot \mathbf{S})_{i-\frac{1}{2}} = (\Pi \cdot (-s_x)\mathbf{i}) = \begin{bmatrix} \rho_{i-\frac{1}{2}} u_{i-\frac{1}{2}} (-s_x) \\ (\rho u)_{i-\frac{1}{2}} u_{i-\frac{1}{2}} (-s_x) + p_{i-\frac{1}{2}} (-s_x) \\ (\rho v)_{i-\frac{1}{2}} u_{i-\frac{1}{2}} (-s_x) \\ (\rho e_T)_{i-\frac{1}{2}} u_{i-\frac{1}{2}} (-s_x) + p_{i-\frac{1}{2}} u_{i-\frac{1}{2}} (-s_x) \end{bmatrix} \tag{2.24}$$

$$(\Pi \cdot \mathbf{S})_{j+\frac{1}{2}} = (\Pi \cdot s_y\mathbf{j}) = \begin{bmatrix} \rho_{j+\frac{1}{2}} v_{j+\frac{1}{2}} s_y \\ (\rho u)_{j+\frac{1}{2}} v_{j+\frac{1}{2}} s_y \\ (\rho v)_{j+\frac{1}{2}} v_{j+\frac{1}{2}} s_y + p_{j+\frac{1}{2}} s_y \\ (\rho e_T)_{j+\frac{1}{2}} v_{i+\frac{1}{2}} s_y + p_{j+\frac{1}{2}} v_{j+\frac{1}{2}} s_y \end{bmatrix} \tag{2.25}$$

$$(\Pi \cdot \mathbf{S})_{j-\frac{1}{2}} = (\Pi \cdot (-s_y)\mathbf{j}) = \begin{bmatrix} \rho_{j-\frac{1}{2}} v_{j-\frac{1}{2}} (-s_y) \\ (\rho u)_{j-\frac{1}{2}} v_{j-\frac{1}{2}} (-s_y) \\ (\rho v)_{j-\frac{1}{2}} v_{j-\frac{1}{2}} (-s_y) + p_{j-\frac{1}{2}} (-s_y) \\ (\rho e_T)_{j-\frac{1}{2}} v_{j-\frac{1}{2}} (-s_y) + p_{j-\frac{1}{2}} v_{j-\frac{1}{2}} (-s_y) \end{bmatrix} \tag{2.26}$$

Equation 2.23 to 2.26 shows explicitly how to calculate the flux of Π in terms of properties in each surface, then this calculation depends on the interpolation of these properties in each surface. The VAT code uses a fourth-order and explicit interpolation scheme derived by Pimenta (2016). This scheme uses a total of four control volumes in interpolation for each surface, two volumes ahead and two behind the surface. The stencil for calculation of surfaces $i + 1/2$ and $j + 1/2$ can be seen in Fig. 2.2b. For a generic property f, the interpolation is computed as

$$f_{i+\frac{1}{2},j} = \frac{9}{16}\left(\overline{f}_{i,j} + \overline{f}_{i+1,j}\right) - \frac{1}{16}\left(\overline{f}_{i-1,j} + \overline{f}_{i+2,j}\right), \tag{2.27}$$

$$f_{i,j+\frac{1}{2}} = \frac{9}{16}\left(\overline{f}_{i,j} + \overline{f}_{i,j+1}\right) - \frac{1}{16}\left(\overline{f}_{i,j-1} + \overline{f}_{i,j+2}\right), \tag{2.28}$$

$$f_{i-\frac{1}{2},j} = \frac{9}{16}\left(\overline{f}_{i-1,j} + \overline{f}_{i,j}\right) - \frac{1}{16}\left(\overline{f}_{i-2,j} + \overline{f}_{i+1,j}\right), \tag{2.29}$$

$$f_{i,j-\frac{1}{2}} = \frac{9}{16}\left(\overline{f}_{i,j-1} + \overline{f}_{i,j}\right) - \frac{1}{16}\left(\overline{f}_{i,j-2} + \overline{f}_{i,j+1}\right), \tag{2.30}$$

where f can assume each value in equations 2.23 to 2.26.

2.4 Artificial Dissipation

The surface interpolation presented in section 2.3 is a centered one, then an explicit artificial dissipation must be included. This dissipation ensures the numerical stability of the code and control of numerical error caused by strong derivatives. Equation 2.16 becomes

$$\Delta\overline{\mathbf{U}}_{i,j} = -\mathcal{F}_{i,j} + \mathcal{R}_{i,j} + \mathcal{D}_{i,j}. \tag{2.31}$$

where $\mathcal{D}_{i,j}$ is the artificial dissipation operator using the basic idea proposed by Jameson, Schmidt and Turkel (1981) where the operator for a control volume is computed by the sum of the operators acting in each surface, in the following way:

$$\mathcal{D}_{i,j} = \left(d_{i+1/2} - d_{i-1/2}\right) + \left(d_{j+1/2} - d_{j-1/2}\right), \tag{2.32}$$

where, for each control surface, a second-order and a fourth-order term are used, so that

$$d_{i+\frac{1}{2}} = \epsilon^{(2)}_{i+\frac{1}{2}}\left[\overline{\mathbf{U}}_{i+1,j} - \overline{\mathbf{U}}_{i,j}\right] - \epsilon^{(4)}_{i+\frac{1}{2}}\left[\overline{\mathbf{U}}_{i+2,j} - 3\overline{\mathbf{U}}_{i+1,j} + 3\overline{\mathbf{U}}_{i,j} - \overline{\mathbf{U}}_{i-1,j}\right], \tag{2.33}$$

$$d_{j+\frac{1}{2}} = \epsilon^{(2)}_{j+\frac{1}{2}}\left[\overline{\mathbf{U}}_{i,j+1} - \overline{\mathbf{U}}_{i,j}\right] - \epsilon^{(4)}_{j+\frac{1}{2}}\left[\overline{\mathbf{U}}_{i,j+2} - 3\overline{\mathbf{U}}_{i,j+1} + 3\overline{\mathbf{U}}_{i,j} - \overline{\mathbf{U}}_{i,j-1}\right], \tag{2.34}$$

$$d_{i-\frac{1}{2}} = \epsilon^{(2)}_{i-\frac{1}{2}}\left[\overline{\mathbf{U}}_{i,j} - \overline{\mathbf{U}}_{i-1,j}\right] - \epsilon^{(4)}_{i-\frac{1}{2}}\left[\overline{\mathbf{U}}_{i+1,j} - 3\overline{\mathbf{U}}_{i,j} + 3\overline{\mathbf{U}}_{i-1,j} - \overline{\mathbf{U}}_{i-2,j}\right], \tag{2.35}$$

$$d_{j-\frac{1}{2}} = \epsilon^{(2)}_{j-\frac{1}{2}}\left[\overline{\mathbf{U}}_{i,j} - \overline{\mathbf{U}}_{i,j-1}\right] - \epsilon^{(4)}_{j-\frac{1}{2}}\left[\overline{\mathbf{U}}_{i,j+1} - 3\overline{\mathbf{U}}_{i,j} + 3\overline{\mathbf{U}}_{i,j-1} - \overline{\mathbf{U}}_{i,j-2}\right]. \tag{2.36}$$

The second-order term acts in high values of divergent, such as chock waves or sound waves, and the fourth-order act in vorticity.

The calculation of the forth-order dissipation operator, $\epsilon^{(4)}_{j-1/2}$, is made with the second-order operator, $\epsilon^{(2)}_{j-1/2}$, and a calibration constant, $K^{(4)}$,

$$\epsilon^{(4)}_{i+\frac{1}{2}} = \max\left[0, \left(K^{(4)} - \epsilon^{(2)}_{i+\frac{1}{2}}\right)\right]. \tag{2.37}$$

The second-order dissipation operator, deviates from the initial proposal of Jameson, Schmidt and Turkel (1981), resulting in

$$\epsilon^{(2)}_{i+\frac{1}{2}} = \max\left[\left(\Psi_{\text{rot}}\right)_{i+\frac{1}{2}}, \left(\Psi_{\text{div}}\right)_{i+\frac{1}{2}}, \left(\Psi_{\text{prs}}\right)_{i+\frac{1}{2}}, \left(\Psi_{\text{den}}\right)_{i+\frac{1}{2}}\right]. \tag{2.38}$$

Calculation in 2.38 is performed using the maximum value between a vorticity-based sensor,

$$(\Psi_{\text{rot}})_{i+\frac{1}{2}} = K^{(2)}_{\text{rot}} \cdot |\nabla \times \tilde{\mathbf{u}}|_{i+\frac{1}{2}}, \tag{2.39}$$

a divergence-based sensor,

$$(\Psi_{\text{div}})_{i+\frac{1}{2}} = K^{(2)}_{\text{div}} \cdot |\nabla \cdot \tilde{\mathbf{u}}|_{i+\frac{1}{2}}, \tag{2.40}$$

a pressure-based sensor,

$$(\Psi_{\text{prs}})_{i+\frac{1}{2}} = K^{(2)}_{\text{prs}} \cdot |\nabla \tilde{p}|_{i+\frac{1}{2}}, \tag{2.41}$$

and a density-based sensor,

$$(\Psi_{\text{den}})_{i+\frac{1}{2}} = K^{(2)}_{\text{den}} \cdot |\nabla \overline{\rho}|_{i+\frac{1}{2}}, \tag{2.42}$$

where $K^{(2)}$ are calibrations constants for each sensor.

2.5 Time Integration

In order to advance equation 2.31 through time, a third order accurate Runge-Kutta method reported by Yee (1997) is used. The method is slited in three stages:

$$\overline{\mathbf{U}}^1_{i,j} = \overline{\mathbf{U}}^n_{i,j} - \left(\mathcal{F}^n_{i,j} - \mathcal{D}^n_{i,j} - \mathcal{R}^n_{i,j}\right), \tag{2.43}$$

$$\overline{\mathbf{U}}^2_{i,j} = \frac{3}{4}\,\overline{\mathbf{U}}^n_{i,j} + \frac{1}{4}\,\overline{\mathbf{U}}^1_{i,j} - \frac{1}{4}\left(\mathcal{F}^1_{i,j} - \mathcal{D}^1_{i,j} - \mathcal{R}^1_{i,j}\right), \tag{2.44}$$

$$\overline{\mathbf{U}}^{n+1}_{i,j} = \frac{1}{3}\,\overline{\mathbf{U}}^n_{i,j} + \frac{2}{3}\,\overline{\mathbf{U}}^2_{i,j} - \frac{2}{3}\left(\mathcal{F}^2_{i,j} - \mathcal{D}^2_{i,j} - \mathcal{R}^2_{i,j}\right). \tag{2.45}$$

2.6 Immersed Boundary Method

For boundary conditions, VAT uses an immersed-boundary method, that consists of applying boundary conditions into the control volumes where the points of geometry lay on. The imposed conditions for boundary are of null derivatives in the normal direction:

$$\frac{\partial \rho}{\partial x_n} = \frac{\partial \mathbf{u}}{\partial x_n} = \frac{\partial p}{\partial x_n} = 0. \tag{2.46}$$

The directional derivatives of a property f can be calculated as the projection of the gradient of this property in the direction $\mathbf{n}$, which leads

$$\frac{\partial f}{\partial x_n} = \nabla f \cdot \mathbf{n} = n_x \left(\frac{\partial f}{\partial x}\right) + n_y \left(\frac{\partial f}{\partial y}\right) \tag{2.47}$$

To calculate these derivatives, a progressive scheme of finite differences is used. For instance, the x-derivative is given as

$$\left(\frac{\partial f}{\partial x}\right)_{i,j} = \frac{1}{12\Delta x}\left(-25f_{i,j} + 48f_{i+1,j} - 36f_{i+2,j} + 16f_{i+3,j} - 3f_{i+4,j}\right) + O(\Delta x)^4 \quad (2.48)$$

Consequently, it is possible to calculate the value that property f must assume in the boundary volume control to make null the derivative

$$f_{i,j} = \frac{1}{25}\left(48f_{i+1,j} - 36f_{i+2,j} + 16f_{i+3,j} - 3f_{i+4,j}\right) + O(\Delta x)^4, \quad (2.49)$$

$$f_{i,j} = D_i^+ f + O(\Delta x)^4. \quad (2.50)$$

The same rationale can be applied to the y-direction

$$f_{i,j} = D_j^+ f + O(\Delta y)^4, \quad (2.51)$$

and finally, for a boundary control volume,

$$f_{i,j} = \frac{|n_x| D_i^+ f + |n_y| D_j^+ f}{|n_x| + |n_y|}. \quad (2.52)$$

Figure 2.3 illustrates the immersed-boundary method. The black dots are surface points and the black arrows are the normals. The green control volumes are those that contain surface points. An example of the stencil used for one control volume is given and the green arrow is the normal vector in this surface point, yellow is relative to x-component (equation 2.50) and blue is relative to y-component (equation 2.51).

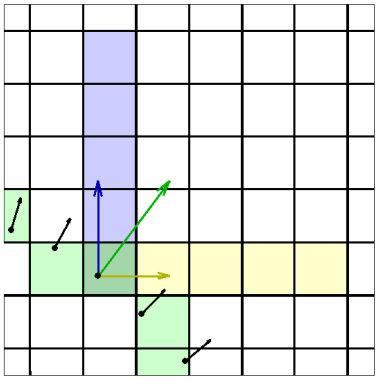

Figure 2.3 – Illustration of immersed boundary method.

The Cartesian mesh is composed of a regular region and a stretched region. The regular region is a rectangle where the geometry is inserted and where is the interest of

simulation. The stretched region, however, is necessary for giving a large amount of inertia to the fluid and represent a large field, where the waves can propagate.

2.7 Computational Implementation

The present work uses VAT, a source-code developed at the Computational Aeroacoustic Laboratory (CAALab) of the University of Brasilia. This code was extensively used in other works (PIMENTA; MISERDA, 2019; MISERDA; PIMENTA; ROCHA, 2020), however, a few changes were done in the code, and this section discusses briefly the contribution of this work. In the first place, the VAT was never used for internal flow simulation. Previous simulations were carried with external flow only. Regarding this fact, the code prohibited geometry points from being outside the regular domain. For internal flow, however, it was necessary to extend the channel for all the computational domain, in both regions, regular and stretched.

Another added feature was the wall imposition. VAT already had the isentropic pressure source, but imposing this condition in a wall requires attention to one detail: the isolation layer. Preliminary simulations using this concept showed vorticity generation at the pressure source, this happened due to the fact the boundary conditions are imposed in two layers. This issue was solved with a second layer in the isentropic source.

The Euler equations are used to model the aeroacoustic flow field in order to investigate physical mechanisms of sound attenuation present in nonlinear acoustics that is not associated with the dissipative nature of the viscous terms present in the Navier-Stokes equations. Besides, solving the Euler equations using an immersed boundary method to impose the geometry of the liners and the channel results in a very fast numerical solver that is highly parallel, using the MPI and OpenMP parallel processing paradigms, as well as the SIMD vectorization directives available for the later. The linearly-distributed sources, placed at the upper and lower walls at the exit of the channel, allows for the generation of N-waves and, also, avoid the numerical reflections at the inlet or outlet of the channel and, thus, avoiding the usage of sponge-zone boundary conditions at that locations. A large number of resonators in the arrays, in combination with the high subsonic flow, was used to generate a liner self-noise with N-wave characteristics, similar to ones observed in rotor-stator interaction and MPT noise.

Three test cases are investigated with increasing complexity. Firstly, a straight channel with the flow and a nonlinear source, then a lined channel with the subsonic flow, and finally, a lined channel with the flow and a nonlinear source. Time and frequency domain results are obtained from measurement probes along the channel in addition to the visualization of the aeroacoustic field throughout the computational domain. It is shown that the proposed approach can effectively simulate nonlinear responses due to the source excitation and the interaction with the liners. It is also able to capture the acoustic

attenuation of tone noise produced by a nonlinear source in a high subsonic flow when an array of cylindrical liners is used.

Chapter 3 will present some results, including results that lead to the modifications cited in this section.

3 Numerical Results

In this chapter, a numerical approach is proposed to investigate a lined array of resonators under both high subsonic flow and pressure. Firstly, the case of a single resonator is investigated under various conditions, presented and shortly discussed as cases 1 to 13 in terms of the numerical setup and field visualization, in order to gain a physical and numerical understanding of the problem before tackling the more complex case. In the setup figures, the following color pattern is used: black for geometry points, blue for pressure injection, cyan for velocity injection, red for probes, and green for the boundary of the regular domain.

The aeroacoustic field visualization variable is defined by

$$\beta_T = \sqrt[10]{|\nabla T|}, \tag{3.1}$$

where $|\nabla T|$ is magnitude of the temperature gradient. This variable allows showing simultaneously sound waves, shocks, and vortical structures, for instance, which are components of the aeroacoustic phenomena with energy levels orders of magnitude apart.

3.1 Single resonator

3.1.1 Case 1

The first presented case in this chapter is a preliminary test. Without prior knowledge in simulating acoustic liners, the first simulations served as the first steps in understanding what would be necessary. Figure 3.1a presents the numerical setup with 40×60 cm in the regular region for this case. A single Helmholtz resonator with 20×20 cm of size and 2×1 mm in the neck, placed in a channel 20 cm high with no flow. The sinusoidal pressure source with 1000 Pa of amplitude and 470 Hz of frequency, shown in blue, covers the channel section aiming to generate plane waves.

Figures 3.2 shows two different moments. Figure 3.2b is the evolution of 3.2a, it is possible to see a perturbation that started in the neck and travels throughout the surfaces. This is an error. Figure 3.1b shows in detail the resonator's neck. The neck is too thin and it led to an isolation problem. Next simulations were carried with a thicker neck.

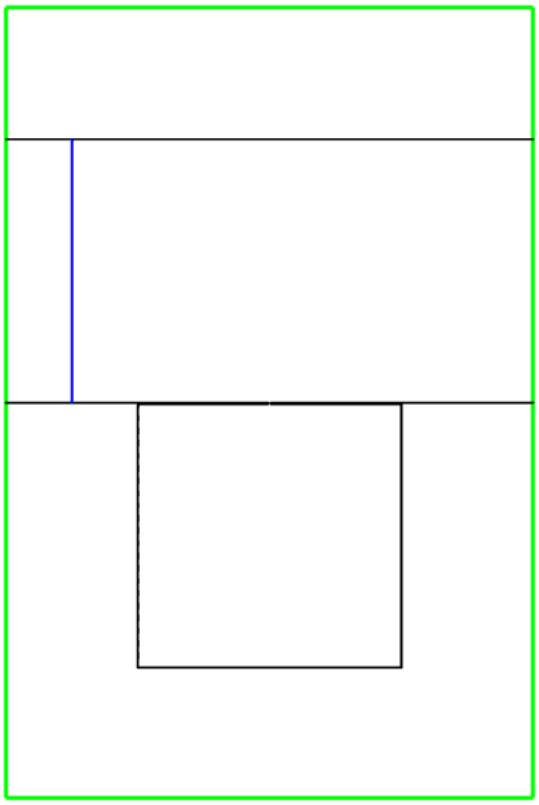

(a) Numerical setup overview.

(b) Neck detail.

Figure 3.1 – Numerical setup for case 1.

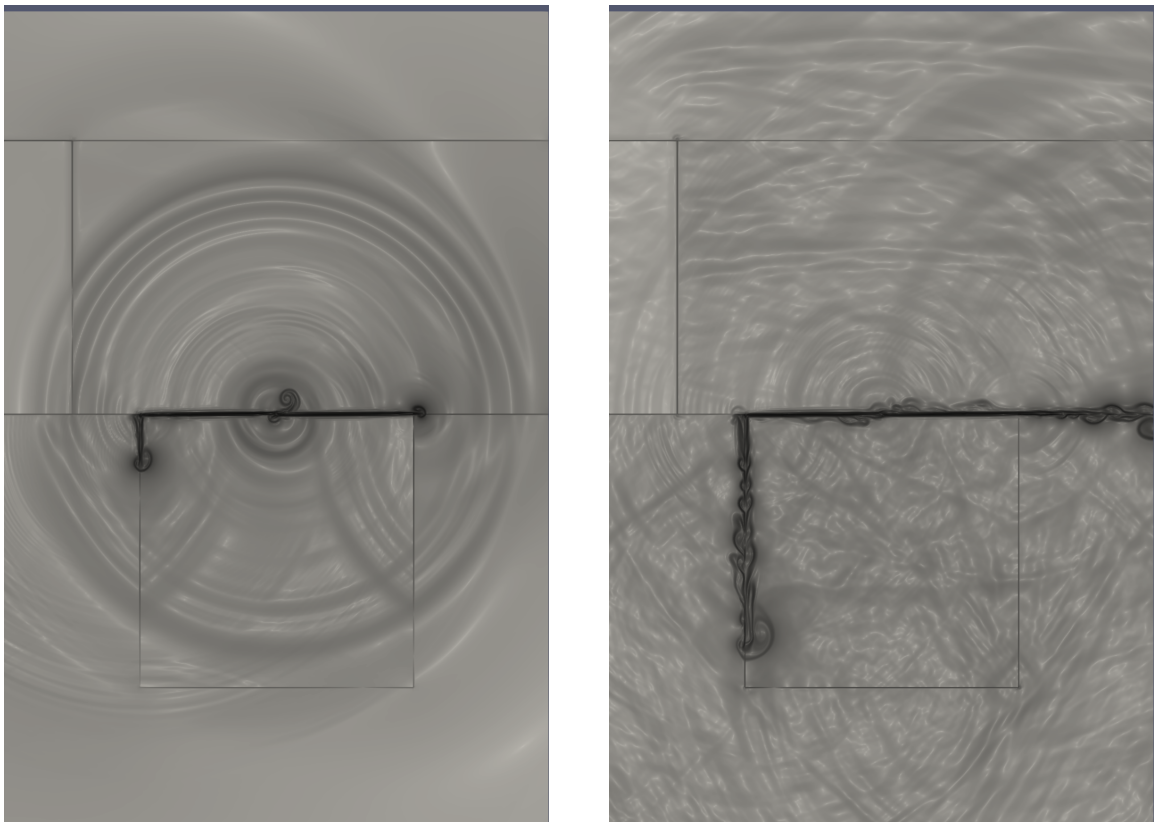

(a) (b)

Figure 3.2 – Visualization with β_T for case 1.

3.1.2 Case 2

This case is similar to case 1: no flow and a pressure source imposing a sinusoidal signal with 1000 Pa of amplitude and 1330 Hz of frequency. The channel has 9 cm of height and the resonator has 5×5 cm with neck of 2×2 mm. Figure 3.3 shows the setup with 20×20 cm of regular region. It is possible to see, in Figures 3.4, the perturbation present in Case 1 is not present here. Figure 3.6a is close to the beginning of the simulation and shows two dark bulbs in the neck. The high pressure generated by the source led to an inlet jet and the low pressure led to an exhaust jet. Figure 3.4b, an evolution of simulation, shows vorticity in the corner of the channel. The geometry here is not closed and possibly can cause unexpected behavior.

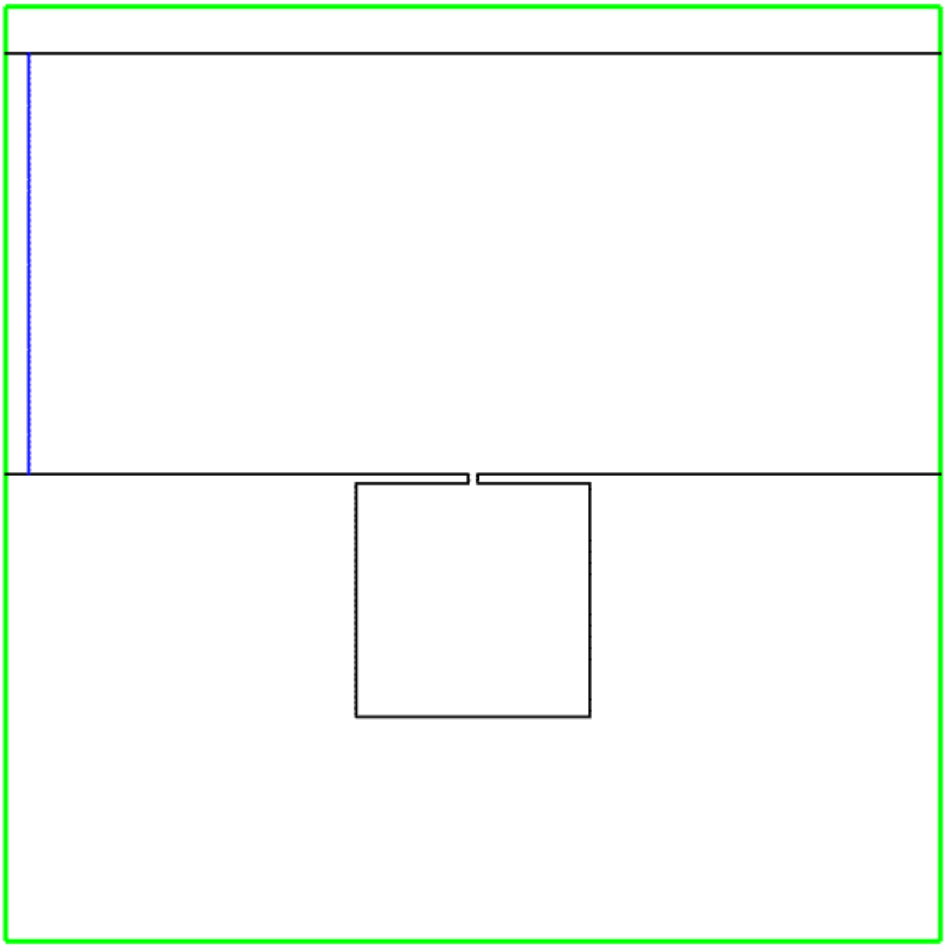

Figure 3.3 – Numerical setup for case 2.

(a) (b)

Figure 3.4 – Visualization with β_T for case 2.

3.1.3 Case 3

Figure 3.5 shows a closed geometry, different from previous geometries. The other parameters are the same from Case 2. In figure 3.6a is possible see a similar topology, with the inlet/exhaust jets. Figure 3.6b, although, shows a vortical structure in the resonator and also vortices in the channel corners.

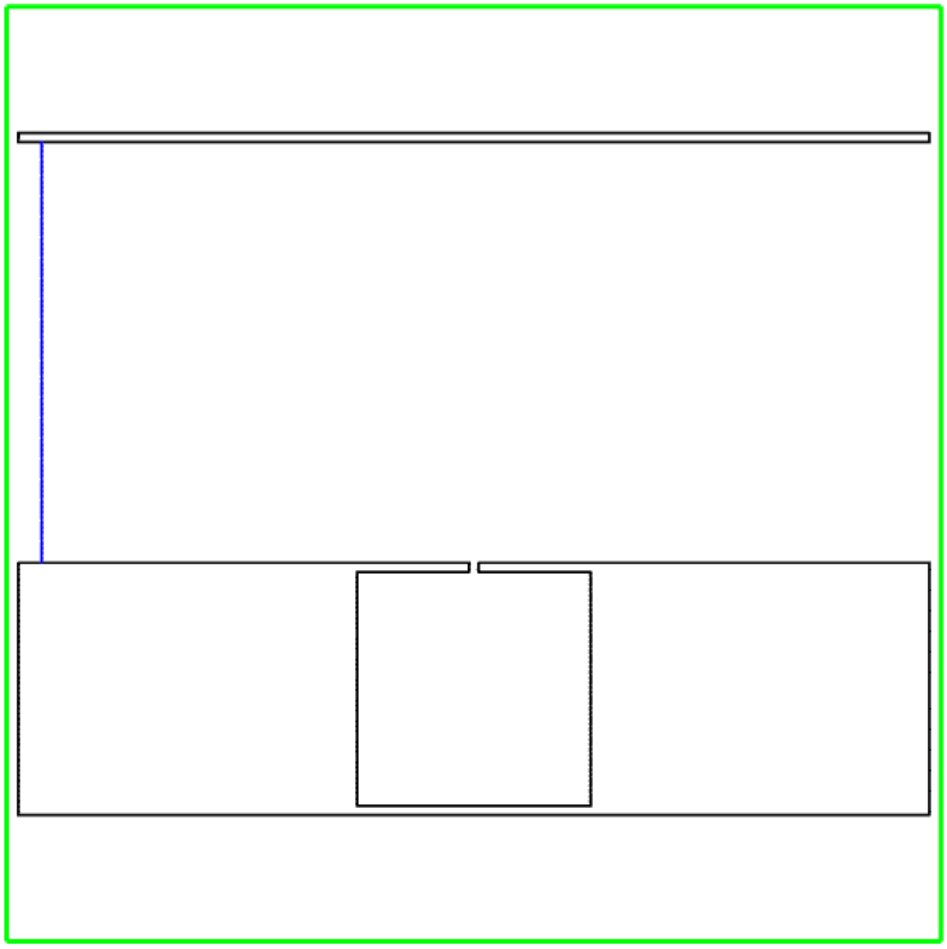

Figure 3.5 – Numerical setup for case 3.

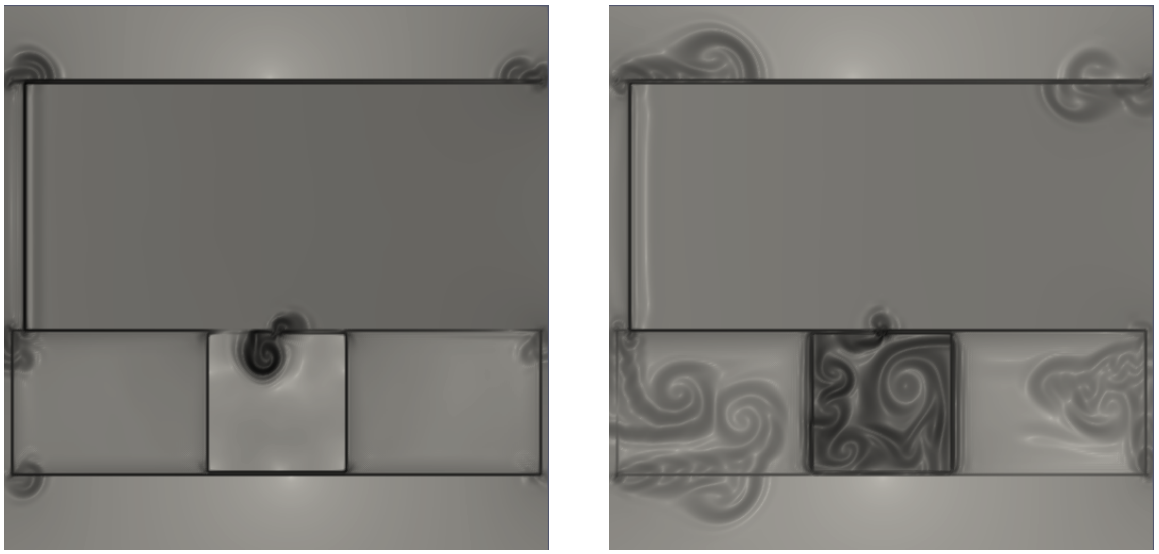

(a) (b)

Figure 3.6 – Visualization with β_T for case 3.

3.1.4 Case 4

The objective of this work requires high flow speed and high-pressure waves. Until this moment, there is no simulation with velocity. In this case, instead of a pressure source, a velocity injection is present. The source, presented in Figure 3.7 in cyan, imposes a velocity of 2.0831322×10^2 m/s ($Mach$ 0.6) in the channel, accelerating from rest.

Figure 3.8a shows an accelerating frame. The darker wavefront is a gradient from the beginning of the simulation. Figure 3.8b is a frame from after the acceleration. The bright wavefront is the reflection of the wavefront from Figure 3.8a at the end of the channel.

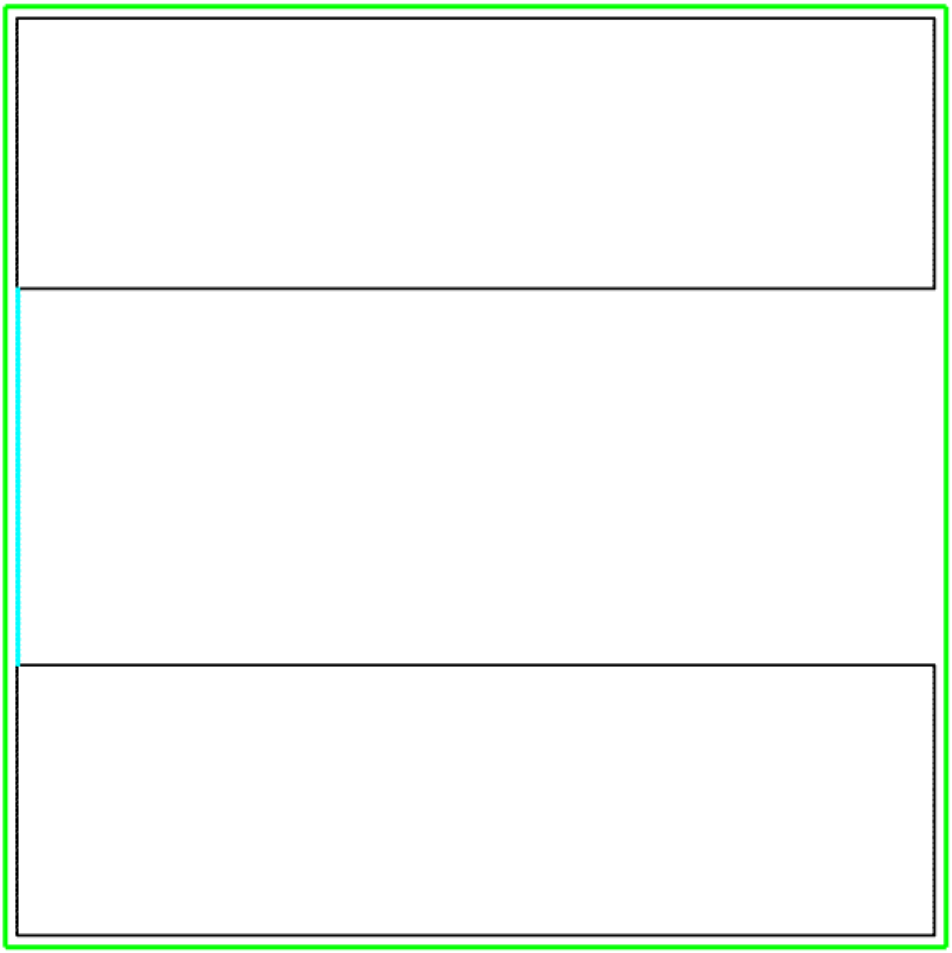

Figure 3.7 – Numerical setup for case 4.

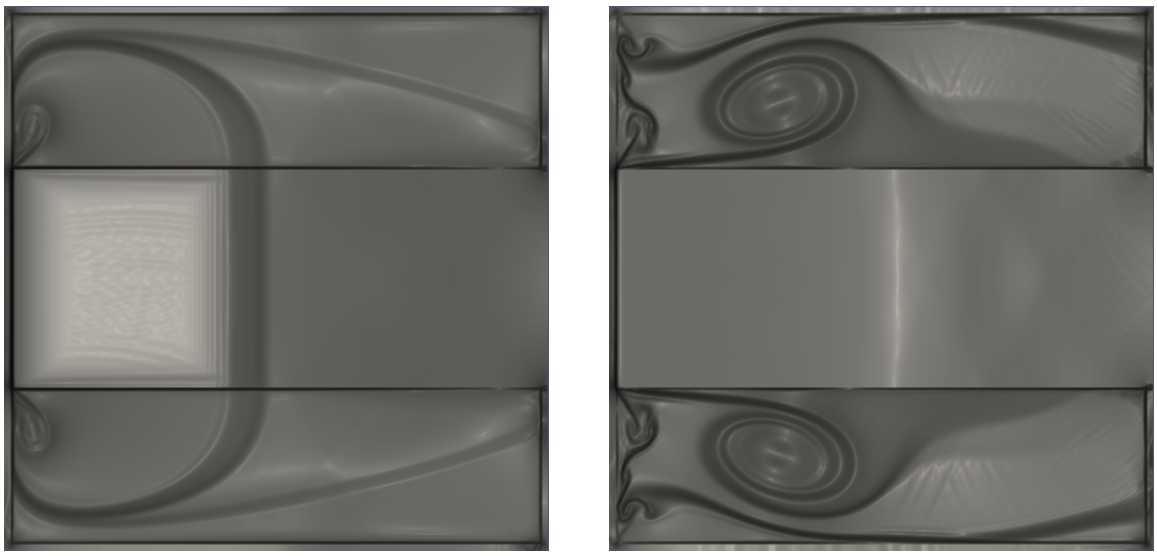

(a) (b)

Figure 3.8 – Visualization with β_T for case 4.

3.1.5 Case 5

In this case, a simple liner is subjected to the flow. The computational regular domain is larger than the previous one with 60×20 cm to accommodate a longer channel. Figure 3.9 shows the setup, with velocity injection at left and a resonator with 4×4 cm and a 2×2 mm in the neck.

Figure 3.10a shows a frame in the acceleration time. The final flow speed is also *Mach* 0.6, however, the acceleration time is double from the previous case, which means a smoother acceleration. In figures 3.10b and 3.10c is possible to see inlet jets at the resonator, generating a vortex with the resonator's size, alternating with exhaust jets, that are advected, besides a high-frequency sound generated at the resonator's neck.

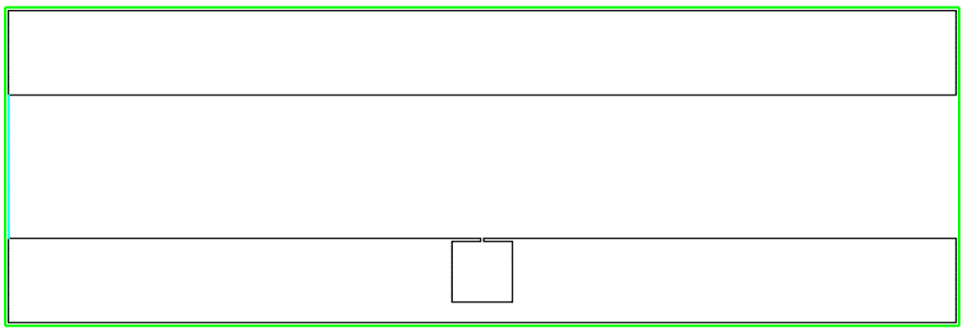

Figure 3.9 – Numerical setup for case 5.

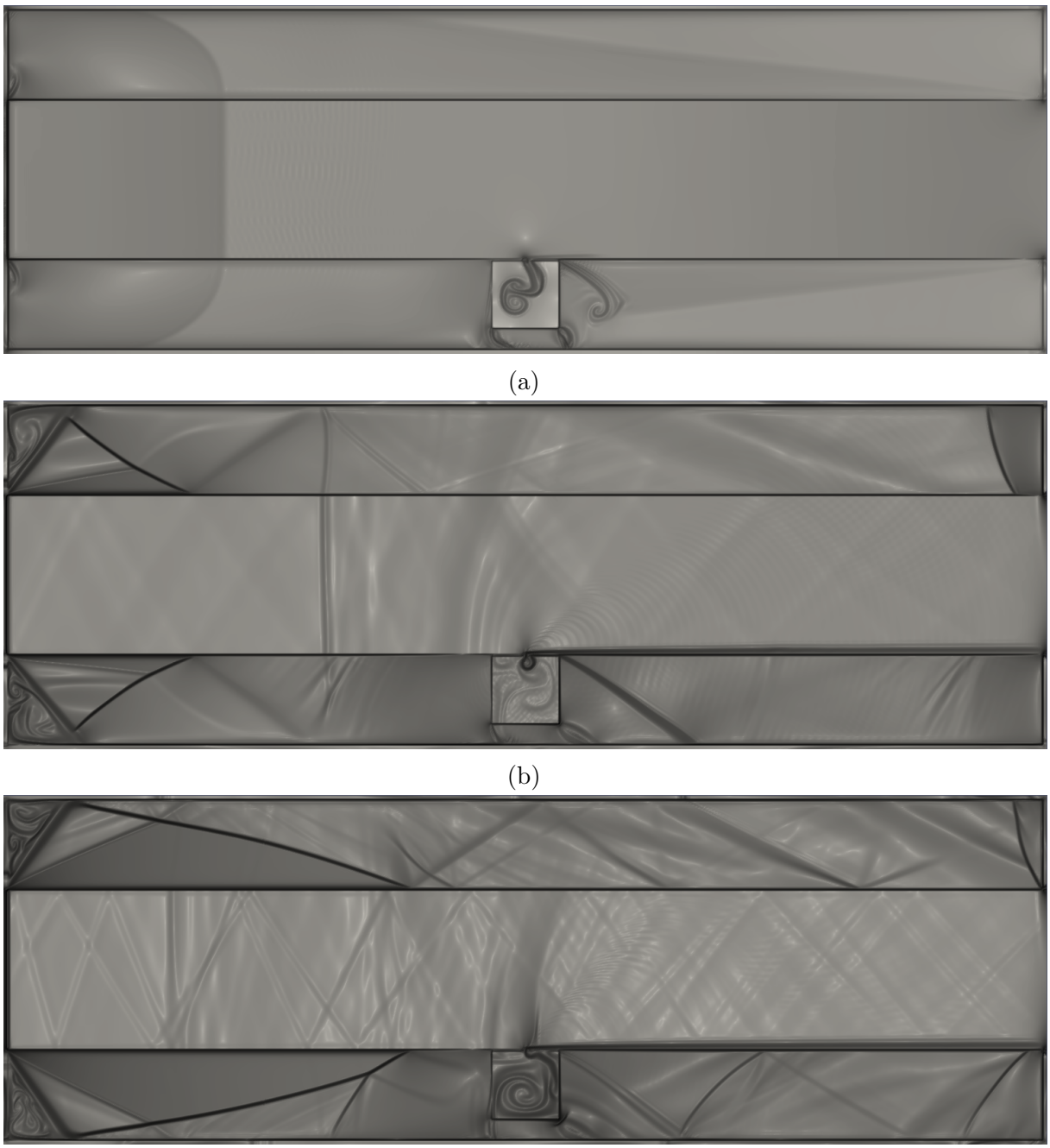

(a)

(b)

(c)

Figure 3.10 – Visualization with β_T for case 5.

3.1.6 Case 6

Cases 4 and 5 present cases with velocity injection at the inlet of the channel. This approach, however, causes reflections in the outlet. In this case, a second source was added to case 4, in the outlet of the channel, as shown in figure 3.11. The presence of the two sources produces in the channel a uniform flow, that can be observed in the white region in Figure 3.12.

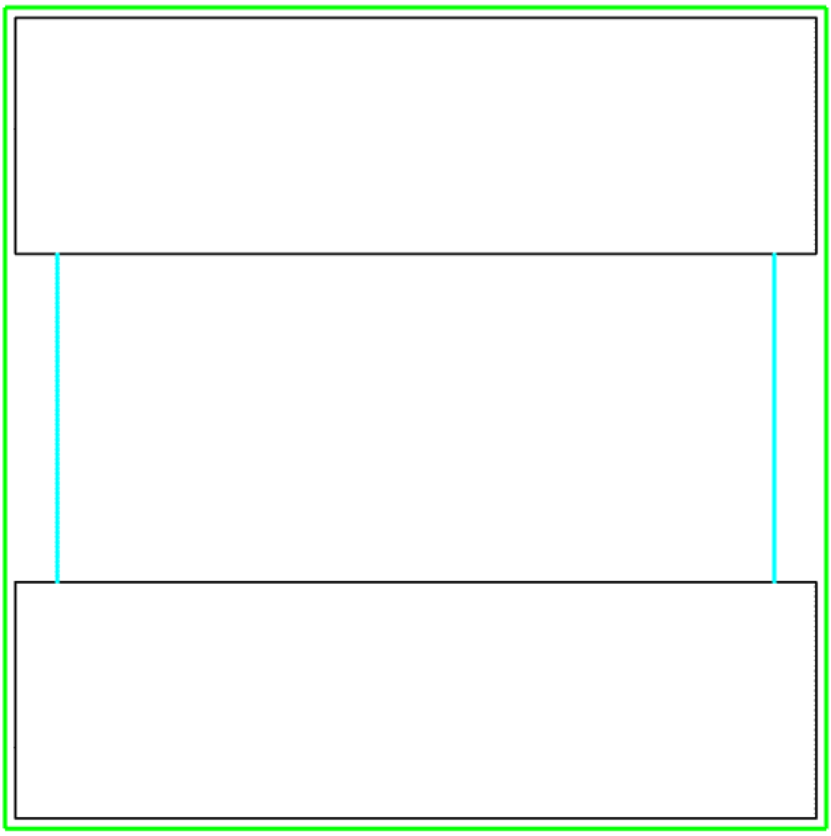

Figure 3.11 – Numerical setup for case 6.

Figure 3.12 – Visualization with β_T for case 6.

3.1.7 Case 7

Based on the results of case 6, this case was designed to see the effects of adding a resonator to the uniform flow of case 5. Figure 3.13 shows the numerical setup for this case.

Figures 3.14a and 3.14b show the results for this case. The general topology is similar to the previous case with a single resonator: inlet/exhaust jets and vortex in the resonator, Figure 3.14a, however, present a wavy structure that generates pressure waves when hits the downstream velocity injection.

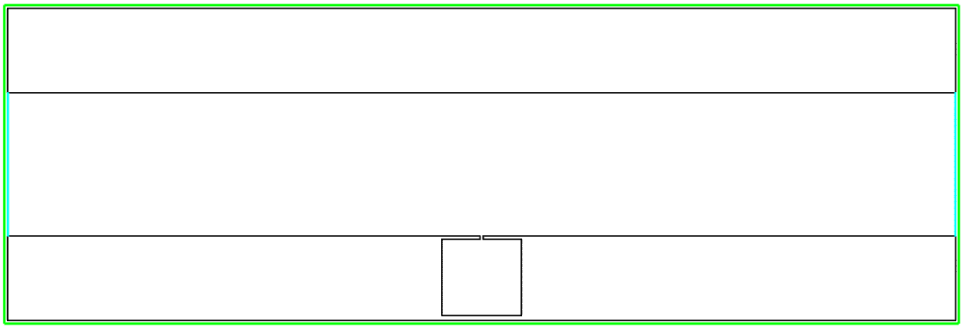

Figure 3.13 – Numerical setup for case 7.

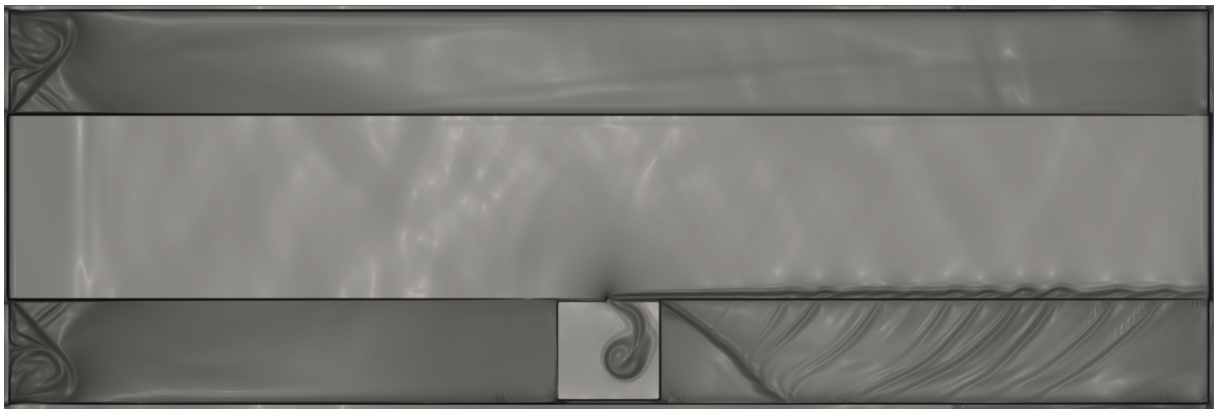

(a)

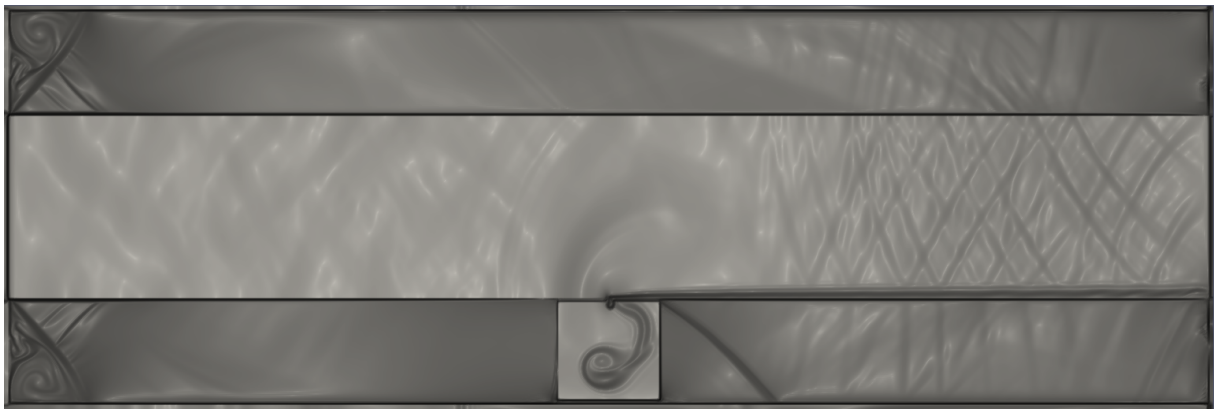

(b)

Figure 3.14 – Visualization with β_T for case 7.

3.1.8 Case 8

Until this point, geometry was limited to the regular region of the domain. In this case, the approach was to extend the channel outside the regular region. With this extension, the usual boundary condition of VAT can be applied, and perturbations are advected. Figure 3.15 shows the numerical setup, with a regular region of 20×20 cm, a resonator with 4×4 cm and 2×2; mm in the neck. The channel is 8 cm high. The points outside the boundary get spaced to fit the stretched control volumes.

Figure 3.16 shows the result for a $Mach$ 0.6 flow. The downstream velocity injection is not present, then there is no reflection in there, although there are reflections in the upstream source.

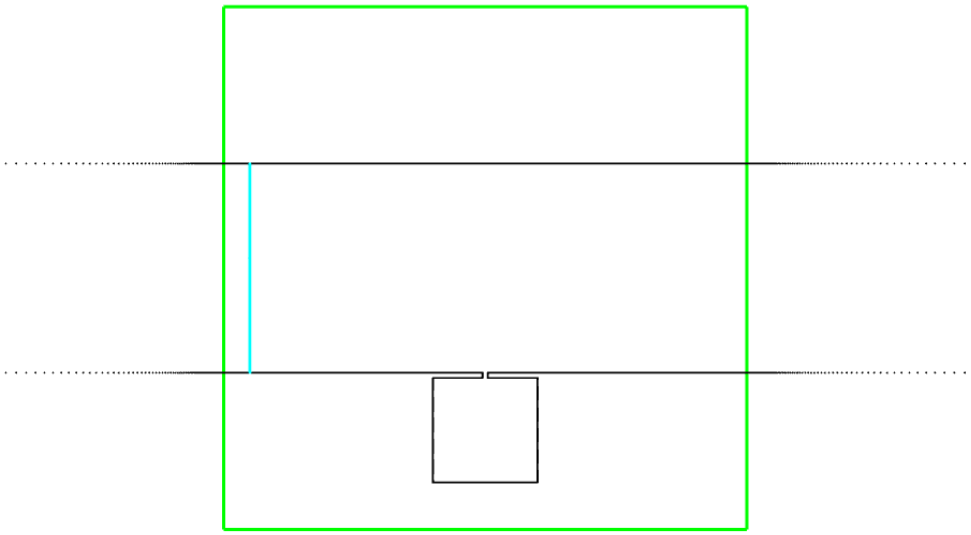

Figure 3.15 – Numerical setup for case 8.

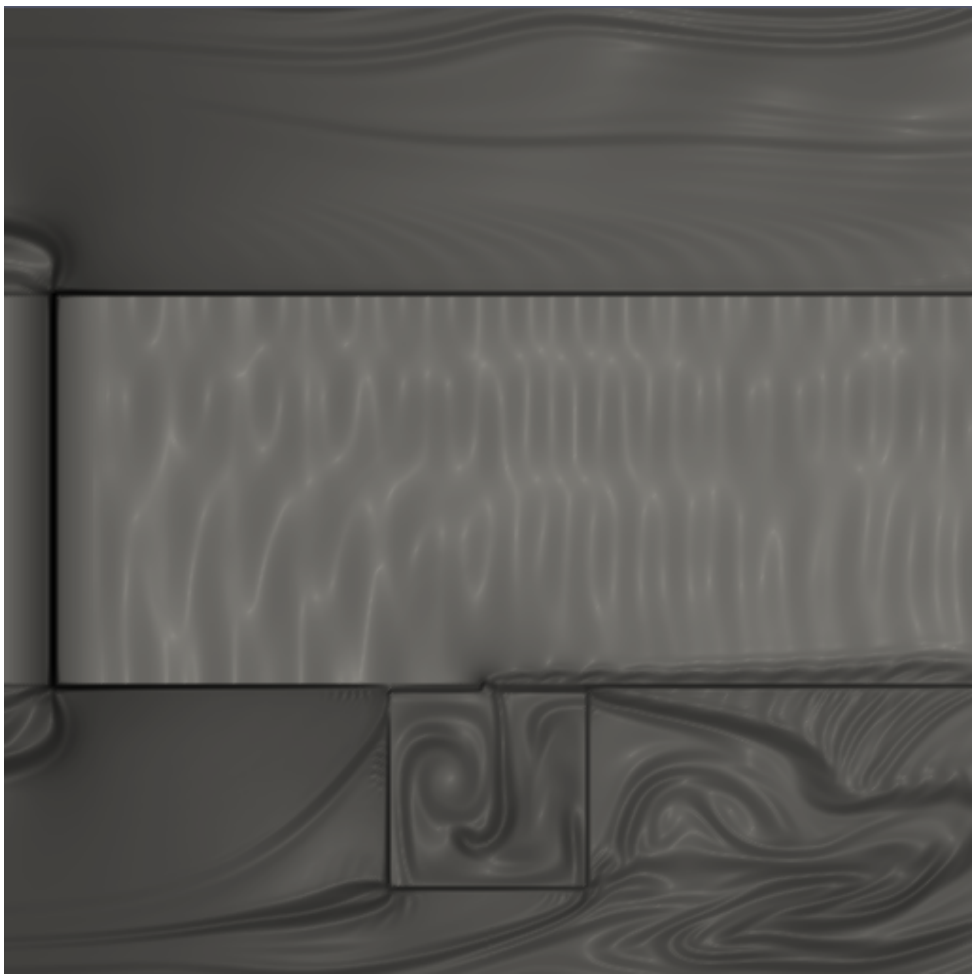

Figure 3.16 – Visualization with β_T for case 8.

3.1.9 Case 9

Concluding that imposing velocity in a section of channel brought some reflections issues, a new way to impose the velocity condition is needed. Extending the channel to the stretched area, however, allowed the use of the default acceleration process, with an inertial force. Figure 3.17 show the setup for this case. The regular region has 20×20 cm, the channel is 8 cm high and a flow is accelerated to $Mach$ 0.6.

Figure 3.18 show the result. The white image shows the complete absence of gradients, which means that this idea can be used.

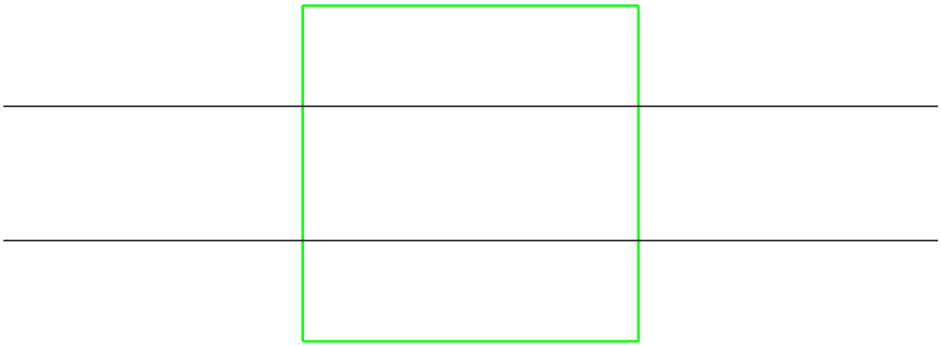

Figure 3.17 – Numerical setup for case 9.

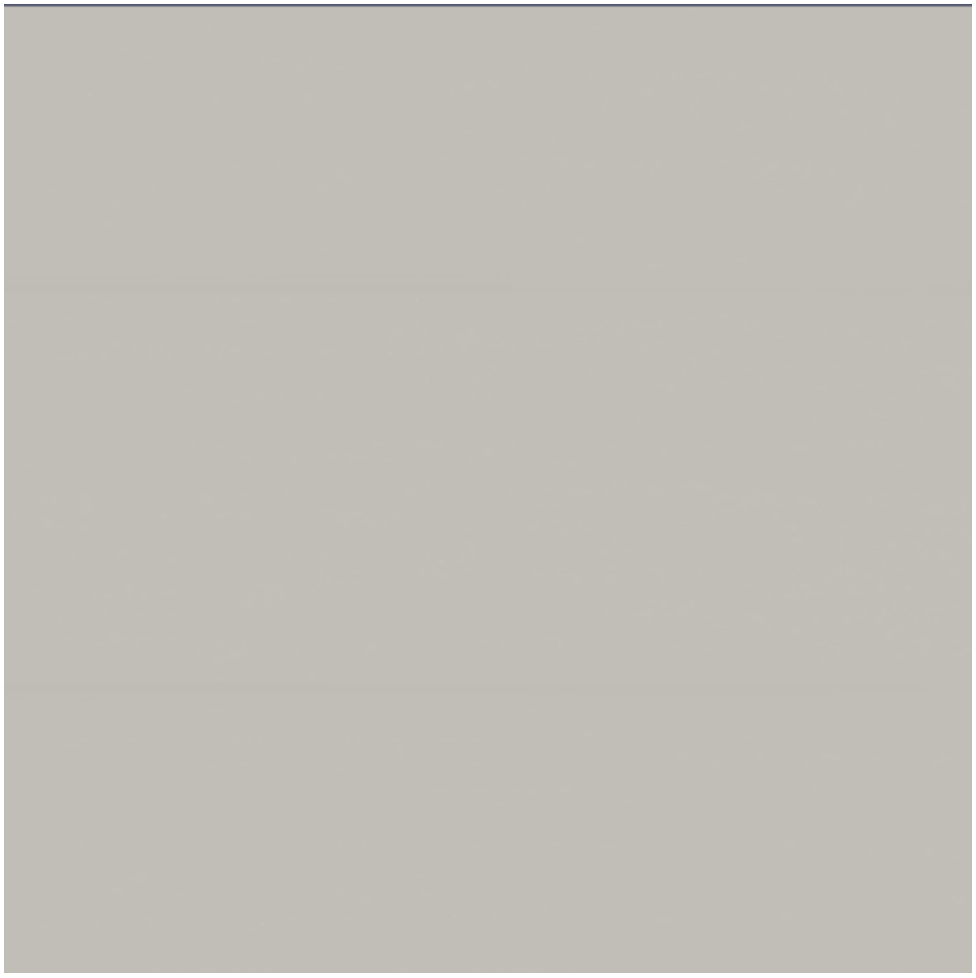

Figure 3.18 – Visualization with β_T for case 9.

3.1.10 Case 10

Figure 3.19 shows the numerical setup for this case. The channel covers all the domain, regular and stretched regions, velocity is set to $Mach$ 0.6 and there is no pressure source. The geometry is the same from case 8.

It is possible to see in the simulation the alternated inlet/exhaust jets. The exhaust jet causes the wavy structure advected shown in Figure 3.20a. Figure 3.20b shows a frame

with an inlet jet, that causes the vortical structure in the resonator. It is possible to see also a wavefront generated when the jet direction changes.

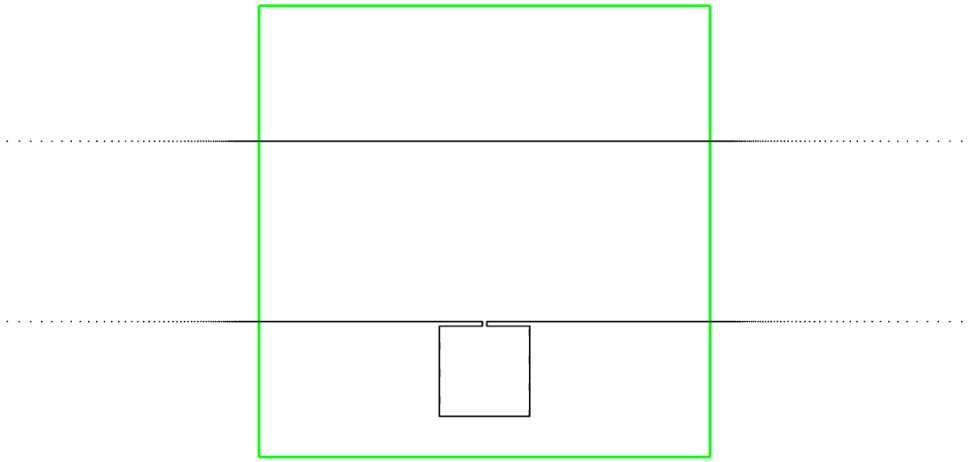

Figure 3.19 – Numerical setup for case 10.

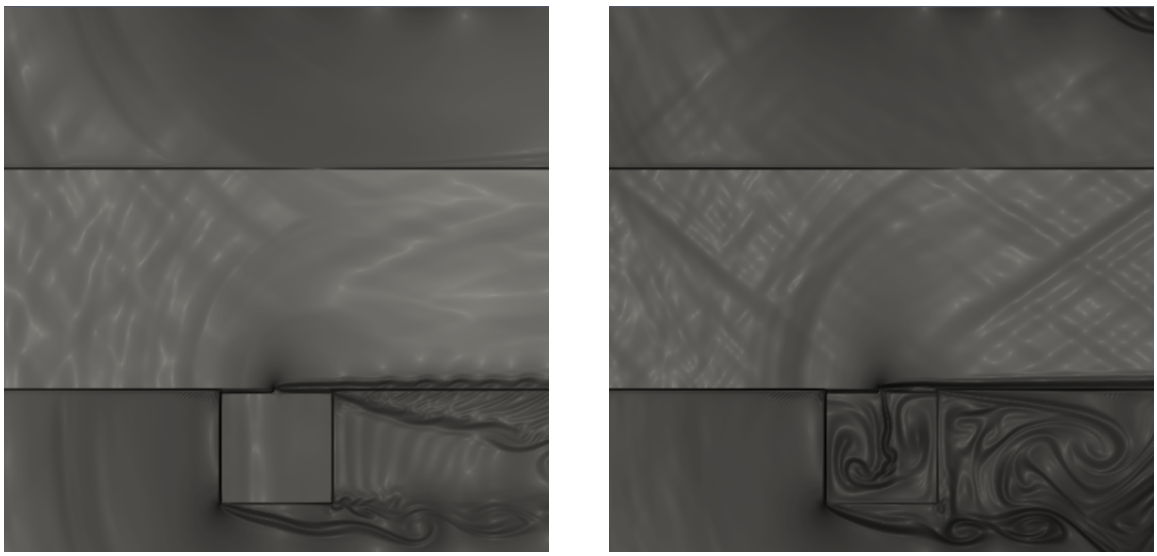

(a) (b)

Figure 3.20 – Visualization with β_T for case 10.

3.1.11 Case 11

With the velocity issue resolved, the pressure is now the focus. Section injection showed not to be a good way for imposing conditions, then in this case the pressure was injected in the channel wall, functioning as loudspeakers. Figure 3.21 shows the distributed pressure sources in blue, with 1000 Pa of amplitude and 10000 Hz of frequency. The channel is 8 cm high and the velocity is set to *Mach* 0.6. Figure 3.22 shows the plane waves generated by the distributed sources.

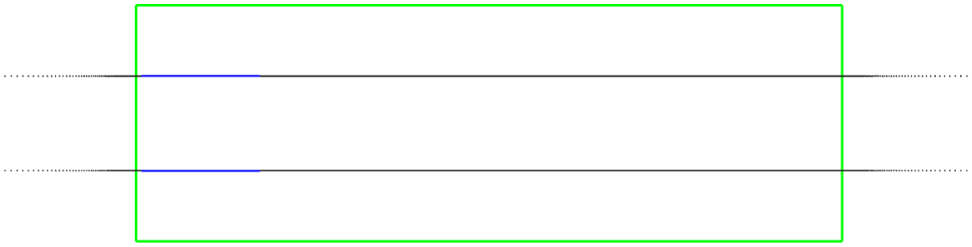

Figure 3.21 – Numerical setup for case 11.

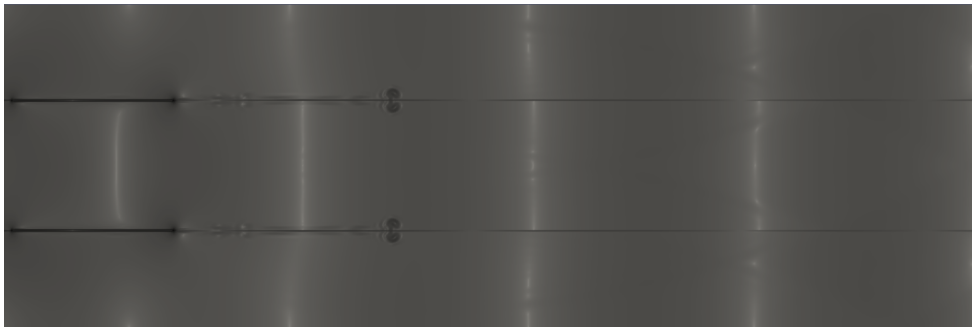

Figure 3.22 – Visualization with β_T for case 11.

3.1.12 Case 12 and 13

This section shows two comparison cases: the first one is a square resonator, the other is a circular resonator. Simulations so far used a square resonator, however, they presented a similar feature: the vortex in the resonator. Figures 3.23 and 3.25 shows the numerical setups for these simulations. The computational domain has the same size, 14×14 cm in the regular region, and the neck has the same position in both cases. The red asterisk shows the position of the probe used for analysis. The square resonator is 3×3 cm and the circular resonator has 3.38 cm of diameter.

Figure 3.24 show a frame of the square resonator simulation. Two different vortices are presented here, and they are present throughout the simulation. The vortices lead to an idea of the circular resonator. Figures 3.26a and 3.26b show the same two vortices inside the resonator, with one difference: unlike the square resonator case, the vortices are not steady. In the circular resonator, the small vortex stays orbiting the big one.

Figure 3.27 presents the spectra for both cases. The square resonator emits a broadband noise, while the circle resonator has a tonal noise.

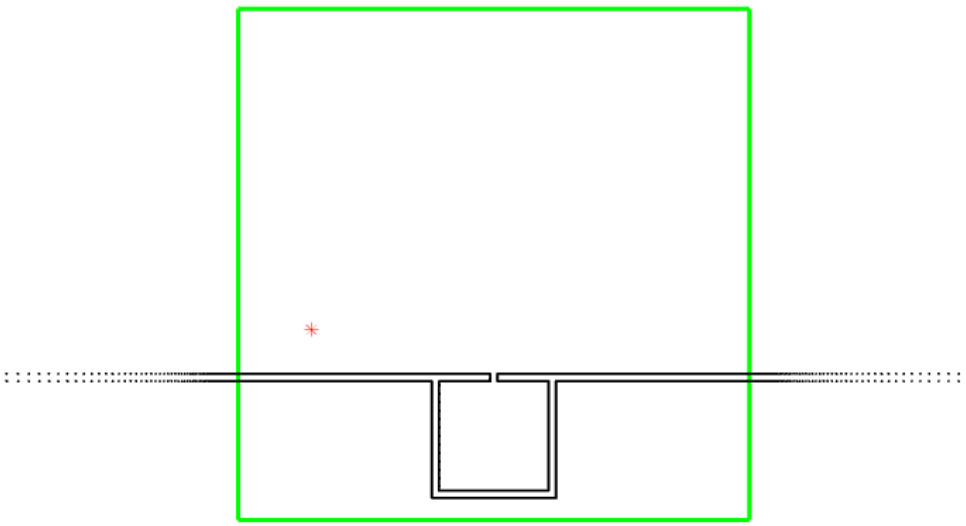

Figure 3.23 – Numerical setup for case 12.

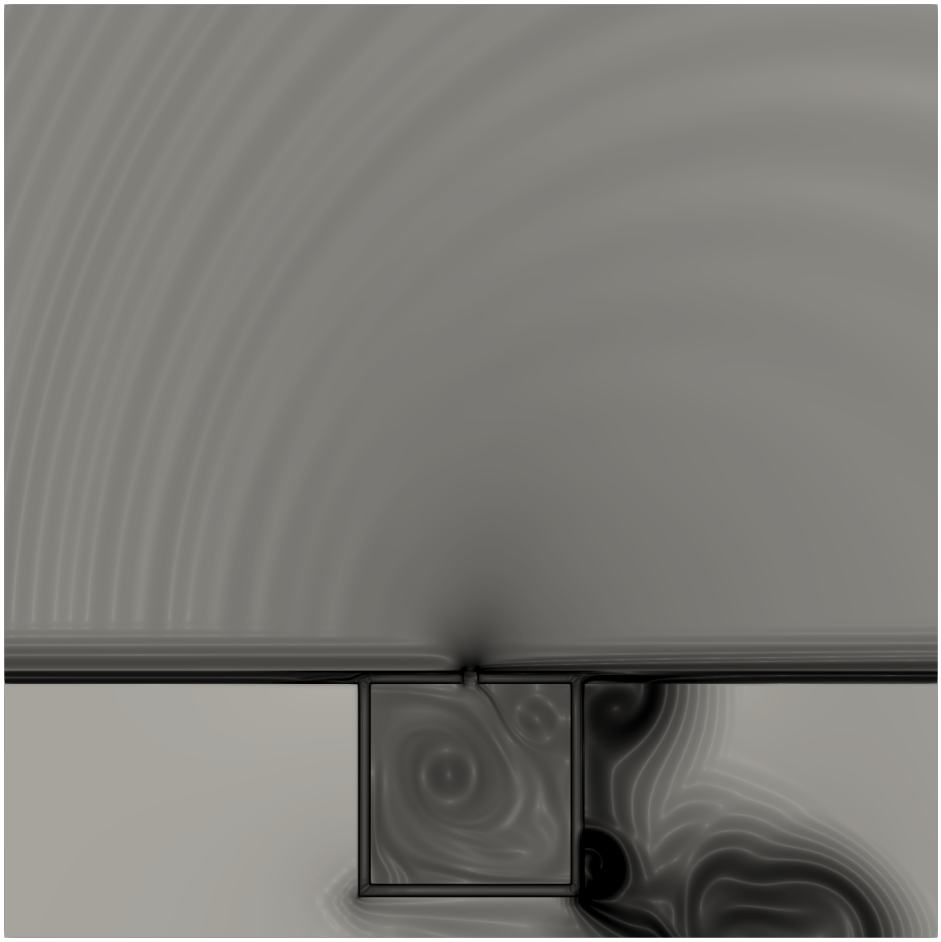

Figure 3.24 – Visualization with β_T for case 12.

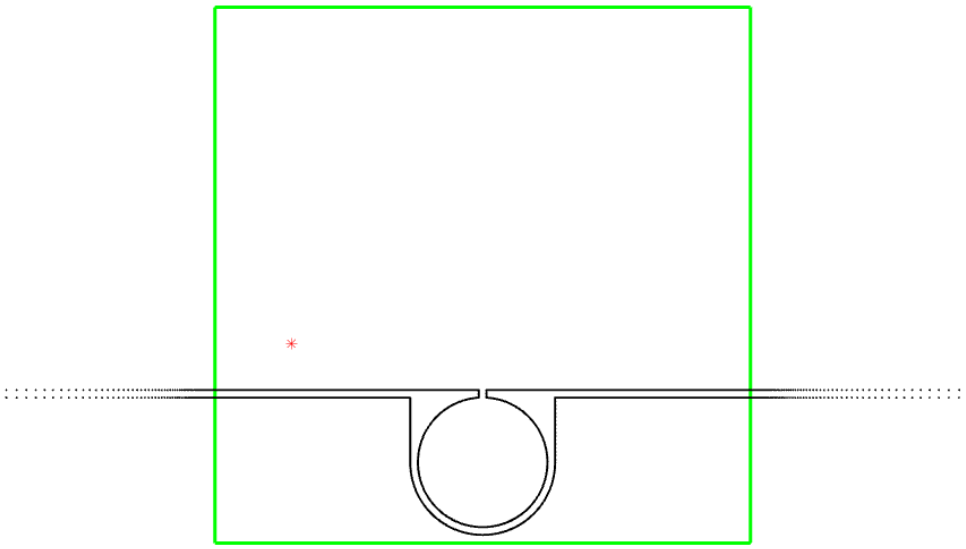

Figure 3.25 – Numerical setup for case 13.

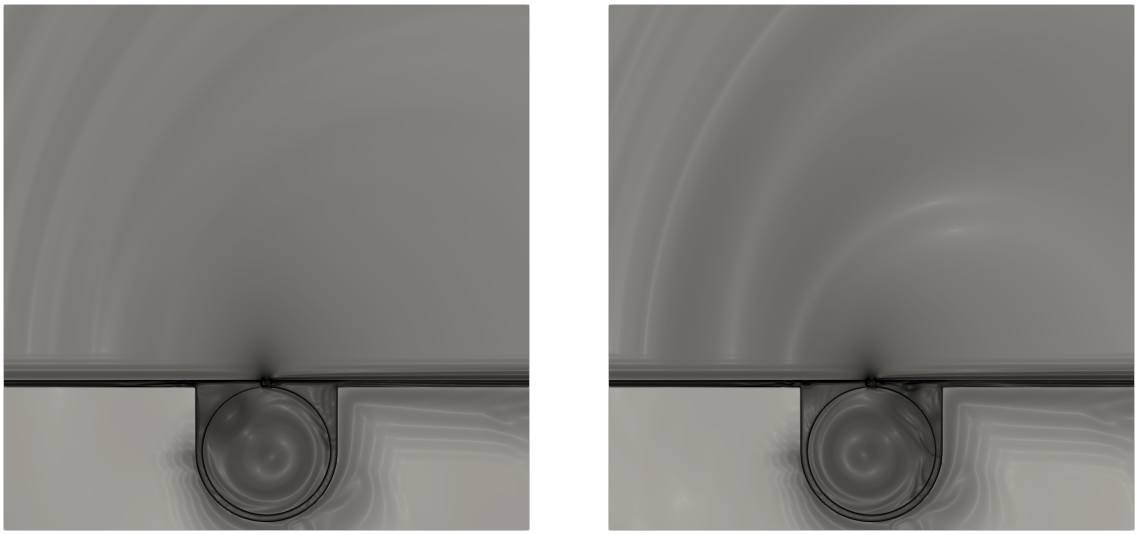

(a) (b)

Figure 3.26 – Visualization with β_T for case 13.

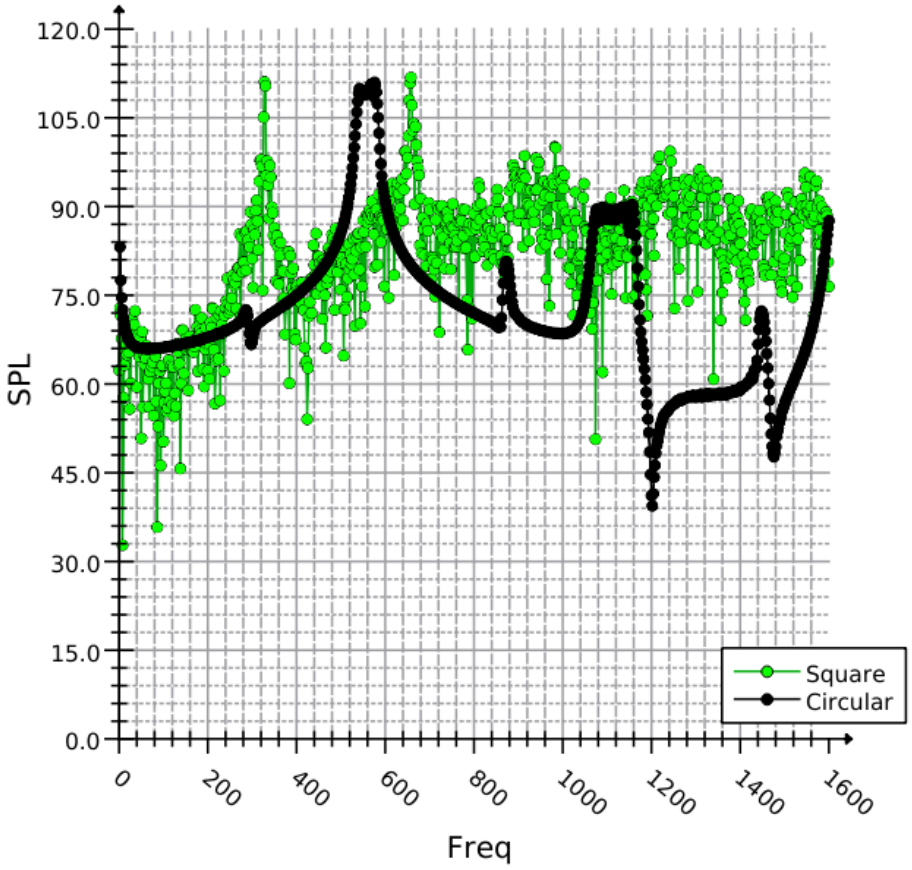

Figure 3.27 – Comparisson between sprectra for circular and square liner.

3.2 Liner configuration

In this section, the numerical setup proposed to investigate the acoustic interaction of a lined array of resonators under both high subsonic flow and pressure is presented. The numerical simulations are performed using a two-dimensional domain, with plane symmetry, over which a plane channel and the upper and lower arrays of cylindrical liners are imposed using the immersed boundary methodology. Figure 3.28a shows the complete geometry of the channel, the locations of the probes, the upper and lower arrays with 15 cylindrical liners each, and the upper and lower linearly distributed sources. Figure 3.28b shows a detailed view of the upper and lower liner arrays and distributed sources.

The linearly distributed sources are composed of a row of finite volumes along the channel wall over which a harmonic pressure fluctuation is imposed. The amplitude of the pressure fluctuation is 1.6×10^4 Pa, and the frequency is 2.25324×10^3 Hz. The corresponding density and temperature fluctuations are calculated using the isentropic relations. The amplitude and frequency of the pressure fluctuations imposed over the sources were chosen, by a trial and error process, to generate a close match, in terms of frequency and sound pressure level for the first harmonic, between the pressure signal

at the channel inlet generated by the flow in a channel, with sources, and the flow in a lined channel, without sources. The numerical results for both cases are presented in the following subsections Flow and source and Flow and cylindrical liners, respectively. The inflow velocity in the channel is 2.0831322×10^2 m/s, the inflow pressure and temperature are 1.01325×10^5 Pa and 3.0×10^2 K, respectively, resulting in an inflow Mach number of 0.6 at the channel inlet. Since the Euler equations govern the flow, with the associated slip condition at the solid boundaries, a uniform velocity profile is established along the channel, without any boundary layer development.

The characteristic length of the setup is the throat width of the cylindrical liner, w (2.0×10^{-3} m), shown in Figure 3.29, where the throat depth d is equal to the width, w. The radius of the cylinder is R and equal to $8.5w$ (17.0×10^{-3} m). The length of the regular computational domain along the channel (horizontal direction) is $1700w$ (3.4 m) and the length in the orthogonal (vertical) direction is $90w$ (0.18 m). The length of the channel is also $1700w$ (3.4 m), while its heigth is $46.1w$ (9.22×10^{-2} m). The linearly distributed sources span along a length of $50w$ (0.1 m).

Figure 3.30 shows the grid resolution for the regular Cartesian mesh and the surface mesh, associated with the immersed boundary methodology, at the throat of the cylindrical liner. Since the throat width is discretized using 10 finite volumes, the total number of these discretization elements in the regular Cartesian grid is 15.3×10^6, where $\Delta x = \Delta y$ (2.0×10^{-4} m). This number is the result of using the same level of grid resolution shown in Figure 3.30 in all the regular domain shown in Figure 3.28a. This level of resolution results in a required time step of 1.0×10^{-7} s to march the numerical solution in time.

Upstream and downstream of the regular computational domain, as well as in both the orthogonal directions, are stretched domains generated using a geometric progression with a common ratio of 1.05. The boundary condition applied at the edges of those stretched domains is a null derivative for all the conservative variables in the normal direction to those edges.

3.2.1 Flow and source

In the following sections, the obtained numerical results are presented for 3 test cases with increasing complexity. Firstly, an airflow from left to right in the channel, with a Mach number of 0.6, and a high-pressure harmonic source distributed at the rightmost part of the channel is considered. Next, the cylindrical liner arrays are included in the geometry near the channel outlet but with no source added. Finally, the linearly-distributed source considered in the first case is considered in addition to the cylindrical liners arrays. The increasing complexity of the flow, source, and liner elements aim to assess, by comparison, their individual effects on the overall sound pressure levels at the inlet of the channel.

Figure 3.31a presents a snapshot of the simulation in the entire computation

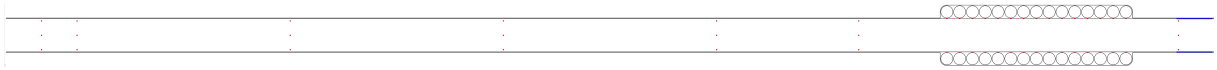

(a) Complete geometry of the 2D channel (black), probes locations (red dots), the upper and lower arrays of cylindrical liners (black), and linearly distributed source (blue).

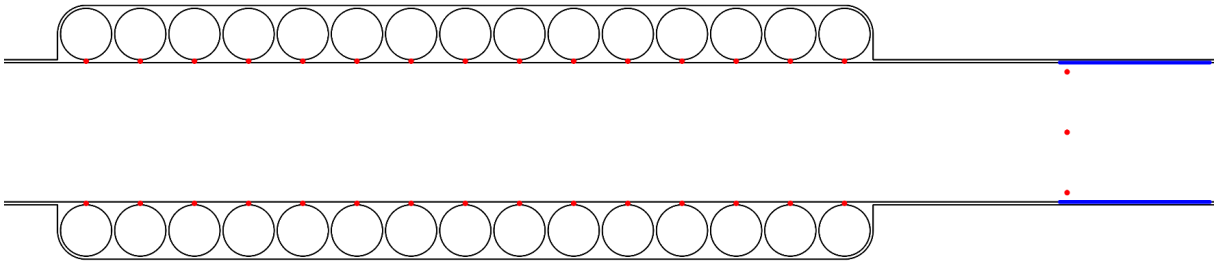

(b) Detail of the geometry at the rightmost part of the 2D channel (black), the upper and lower arrays of cylindrical liners (black), probes locations (red dots), and linearly distributed source (blue).

Figure 3.28 – Geometry the plane channel, the arrays of liners and the distributed source.

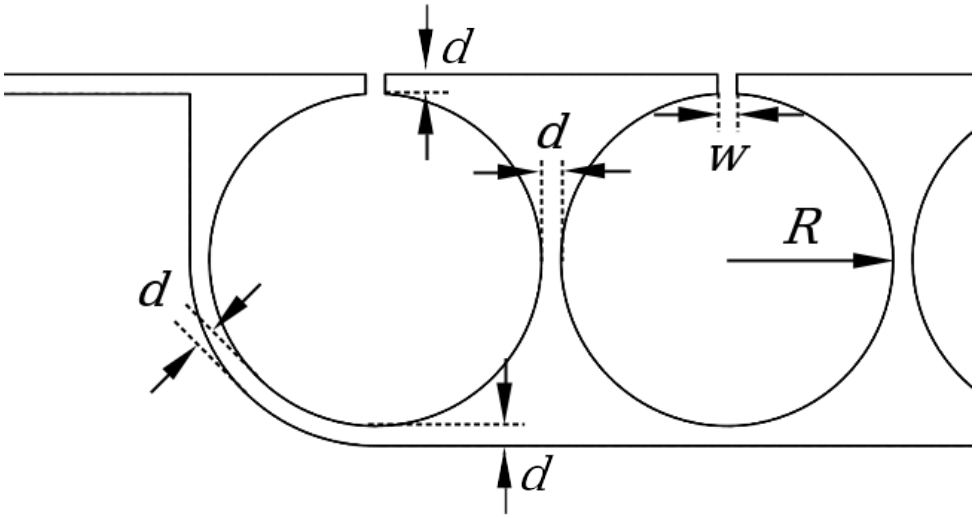

Figure 3.29 – Dimensional parameters for the geometry of the cylindrical liners shown over the left end of the lower array.

domain. It can be noticed that this configuration generates several types of wavefronts, most notably a series of N-waves of high amplitude, which can be seen to be well defined by the vertical lines, associated with the temperature gradient across the shock waves, at Figures 3.31c and 3.31d. Overall, the amplitude of the N-waves decay due to the irreversibility of the shocks, as they propagate upstream from right to left, away from the linearly-distributed sources. From Figure 3.31d, it can be seen that the upper and lower pressure sources interact to generate the N-waves, thus creating the full aeroacoustic field. It can also be visualized the formation of an X-shaped wavefront with a slightly shorter wavelength and a much lower intensity than the N-waves. This structure is probably associated with the height of the channel since it is the distance that separates the upper and lower linearly-distributed sources. Several other additional features can be observed in this field but exploring them is outside the scope of this paper. Figure 3.32 shows a detail

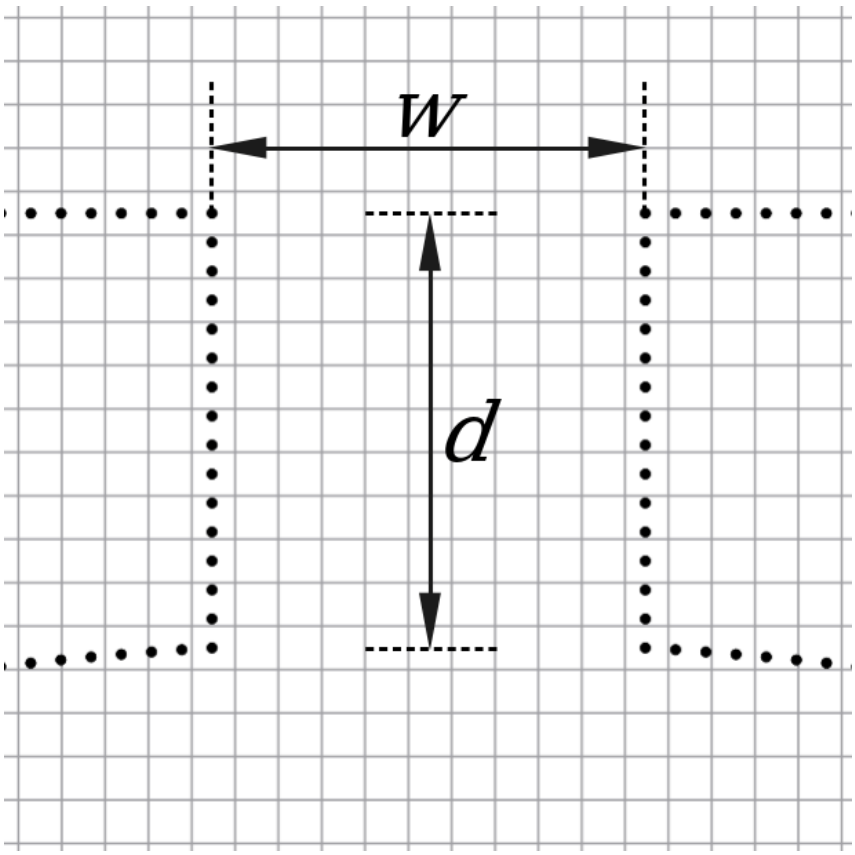

Figure 3.30 – Resolution of the volumetric (Cartesian) and surface grids shown at the throat of the cylindrical liner.

of the time domain pressure response at the inlet of the channel, i.e., the leftmost part of the domain. The high amplitude peaks are related to the dominant N-waves showed in the aeroacoustic field. Other spatial features observed in Figure 3.31a are related to smaller pressure amplitudes peaks in the time domain response.

3.2.2 Flow and cylindrical liners

Figure 3.33a shows the field visualisation variable β_T for the entire regular domain. It can be noticed that the interaction of the upper and lower liner arrays have generated an aeroacoustic field with similar spatial features and shown in the previous case. Most notably, the presence of N-waves of higher amplitude and an X-shaped wave with lower amplitude at the left side of the liner arrays. Details of the leftmost third, central third and rightmost third part of the regular domain are shown in Figures 3.33b, 3.33c and 3.33d, respectively.

The interaction of the liner upper and lower array can be more clearly observed from Figure 3.33d. Notice that the N-wave is gradually generated from the right to the left side of the liner array and then it propagates towards the channel inlet, at the left end. This effect can be attributed to the interaction of the vorticity structures rotating inside the cylindrical resonators, which gradually interact to form such wavefronts. The

(a) Visualization over the entire regular domain.

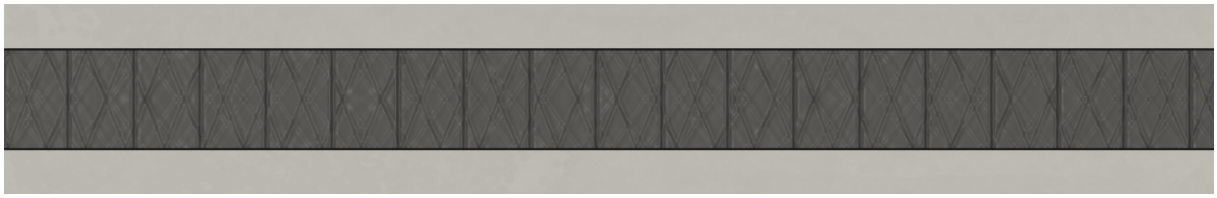

(b) Visualization over the leftmost third of the regular domain.

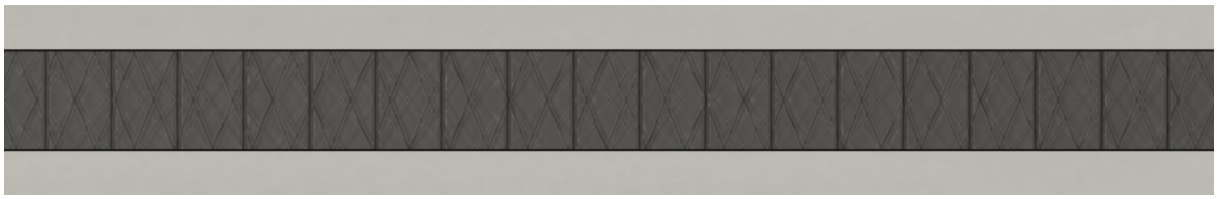

(c) Visualization over the central third of the regular domain.

(d) Visualization over the rightmost third of the regular domain.

Figure 3.31 – Visualization of the aeroacoustic flowfield for the flow and source case.

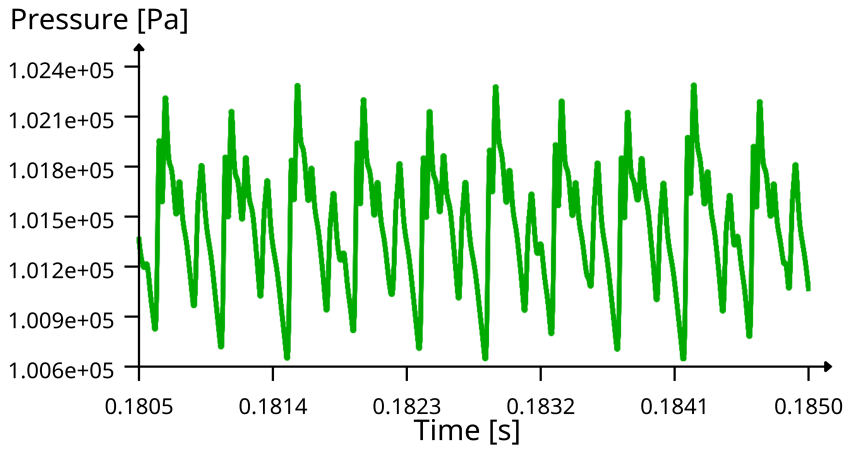

Figure 3.32 – Pressure signal at the inlet of the channel for the flow and source case.

geometry of the resonators is set such that their resonance frequency matches the driving frequency of the harmonic source in the previous case. Consequently, the plane wavefronts have the same or very similar wavelengths. Unlike the previous case, the interaction of the upper and lower cylindrical liners with the aeroacoustic field generates a X-shaped wavefront which is much more significant when compared to the bare channel. Finally, a similar amplitude attenuation is seen as N-waves propagate towards the channel inlet, which can also be attributed to the irreversibility of the shocks. Figure 3.34 present the pressure temporal response at the same location from the previous case. Similarly, the

highest amplitude peaks are related to the dominant N-waves in addition to the lower amplitude features related to the X-shaped wavefronts.

(a) Visualization over the entire regular domain.

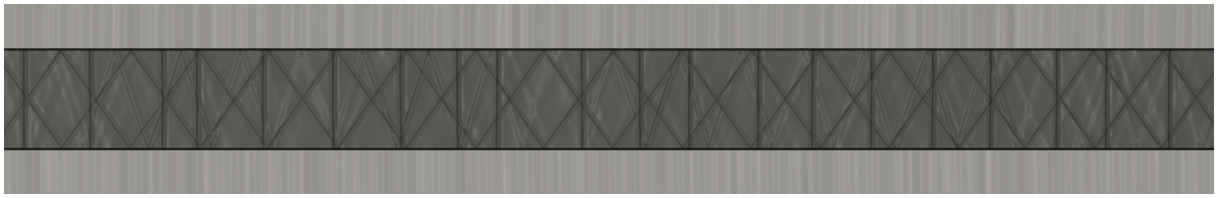

(b) Visualization over the leftmost third of the regular domain.

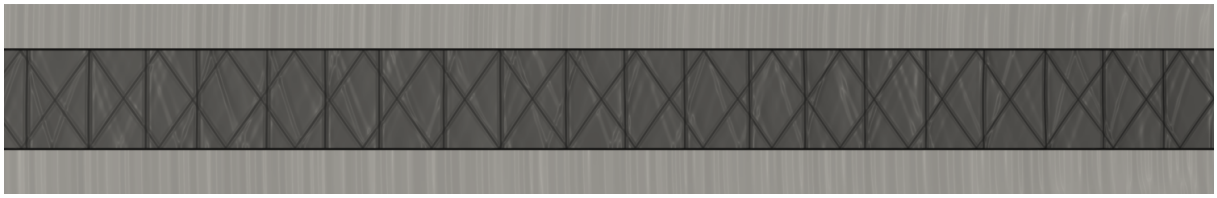

(c) Visualization over the central third of the regular domain.

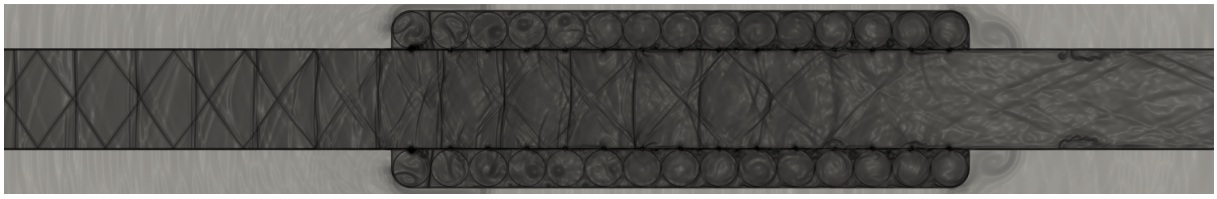

(d) Visualization over the rightmost third of the regular domain.

Figure 3.33 – Visualization of the aeroacoustic flowfield for the flow and cylindrical liners case.

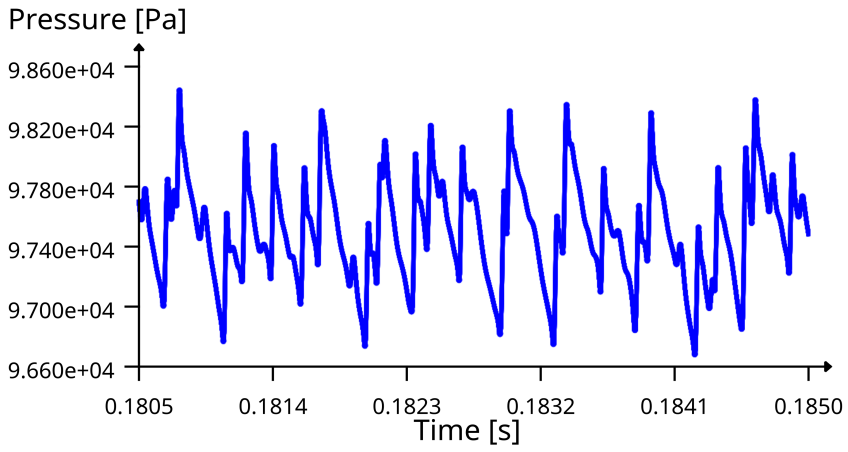

Figure 3.34 – Pressure signal at the inlet of the channel for the flow and cylindrical liners case.

3.2.3 Flow, source, and cylindrical liners

In this last case, the combined effects of the mean flow, the linearly-distributed sources, and the upper and lower cylindrical liners are investigated. Figure 3.35a presents β_T for the entire domain. Similar features from both previous cases can be seen in these results. That is the presence of both the N-waves and the X-shaped wavefronts and their amplitude attenuation as they propagate towards the channel inlet, at the left end. However, the N-waves has been significantly attenuated and thus both wave types present similar amplitudes, as it can be seen more clearly from Figures 3.35b, 3.35c and 3.35d. Figure 3.36 presents the time domain response of the pressure at the channel inlet. Unlike the previous, cases, the amplitude peaks related to the plane wavefront are not dominant in the response and are mixed with other features of the response.

In addition, several important features can be seen Figure 3.35d. It can be noticed that N-waves are generated from the pressure source at the right end, similarly as shown in the first case. This wave propagates towards the liner and it gradually attenuates as it goes through it. Note that this is exactly the opposite effect as shown in the previous case, in which the wave amplitude increased in this direction, as highlighted in Figure 3.37, which shows the aeroacoustic field at the channel outlet for all three cases. Consequently, the wave attenuation can be attributed to the destructive interaction, or phase canceling, of the N-waves generated by the source and the N-waves generated by the cylindrical resonators in the upper and lower liners. As previously stated, the liner arrays have a resonance frequency that is used as the driving frequency imposed on the sources. Moreover, the X-shaped wave is mostly unaffected by the cylindrical liner.

3.2.4 Frequency domain analysis

In this section, the results in terms of sound pressure levels (SPL) from the three previous cases are investigated in the frequency domain. Figure 3.38, 3.39 and 3.40, present the SPL spectrum from 0; Hz up to approximately 20; kHz, bins marked at 2253.24; Hz and its harmonics, for the first, second, and third analyzed cases, respectively, i.e., flow and source only, flow and cylindrical liners and flow, source, and cylindrical liners. For all the spectral power densities presented in these figures, the sampling frequency was 1.0×10^7 Hz which is the inverse of the time step used for the time-marching process of the numerical simulation. The total data length obtained was 2.0×10^6 points for all three cases, but only the last 1.05×10^6 points were used, to eliminate the initial numerical transient of the simulation. A discrete fast Fourier transformation, without windowing, was applied to the reduced data sets.

It can be seen from Figure 3.38, the amplitude peak at 2253.24; Hz is related to the driving frequency of the distributed source and it is related to the N-wave created in this case. Their corresponding higher-order harmonics are noticed by the vertical lines in

(a) Visualization over the entire regular domain.

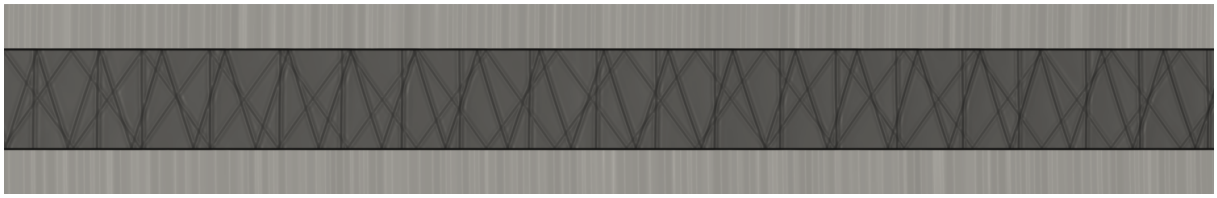

(b) Visualization over the leftmost third of the regular domain.

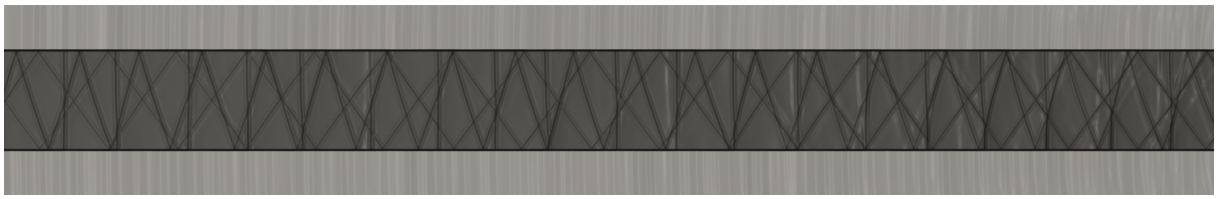

(c) Visualization over the central third of the regular domain.

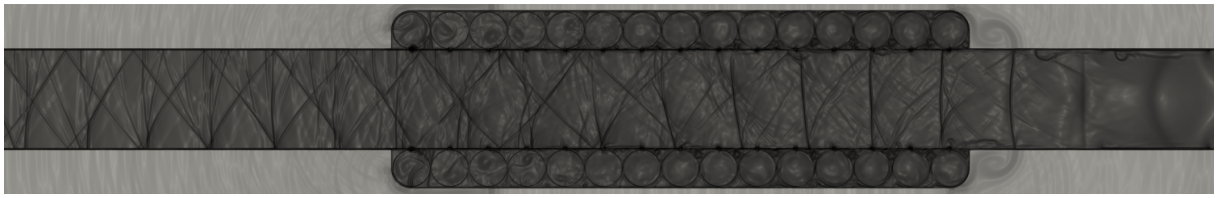

(d) Visualization over the rightmost third of the regular domain.

Figure 3.35 – Visualization of the aeroacoustic flowfield for the flow, source and cylindrical liners.

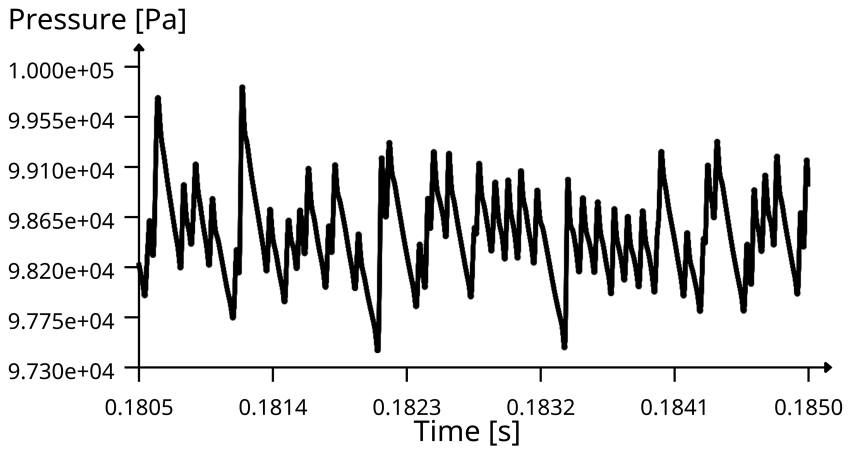

Figure 3.36 – Pressure signal at the inlet of the channel for the flow, source and cylindrical liners.

the plot grid. Also, each horizontal line in the plot grid corresponds to a 3 dB difference. The other amplitude peaks are related to the natural frequencies of the channel and the X-shape wavefronts. Overall, the response spectrum is dominated by the harmonics of the different wave types. From Figure 3.39, it can be seen that broadband behavior is created in the response. It can be attributed to the non-linear interaction of the flow with the cylindrical resonators in the liners. Notice that the frequency peak at 2253.24; Hz is

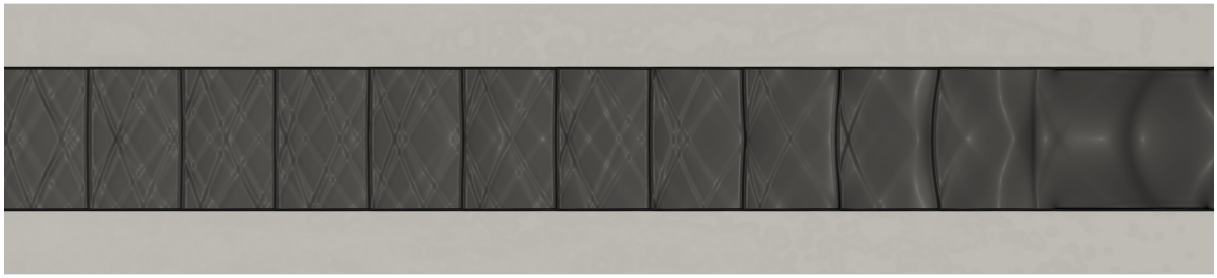

(a) Zoom around the plane channel outlet (right side) with a nonlinear source.

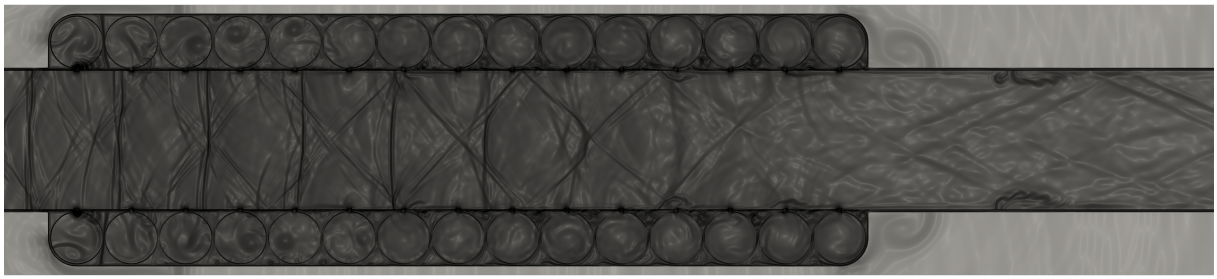

(b) Zoom around the channel outlet (right side) showing the top and bottom arrays of cylindrical liners with no source.

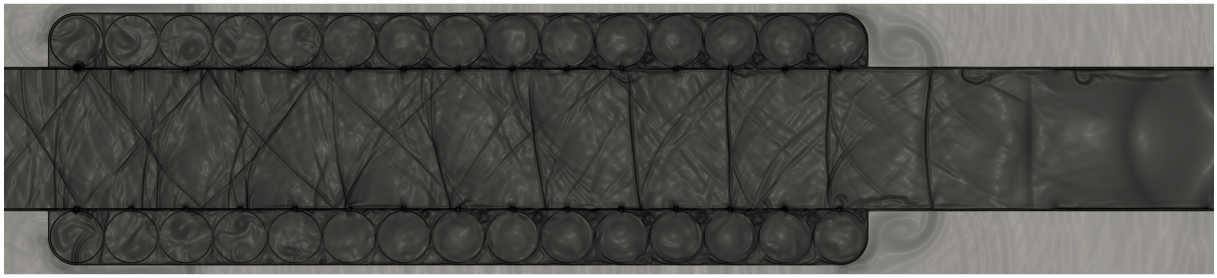

(c) Zoom around the channel outlet (right side) showing the top and bottom arrays of cylindrical liners with a nonlinear source.

Figure 3.37 – Effect of the acoustic treatment over the nonlinear waves.

also present in this case and it is related to the plane wavefront generated, as previously discussed. A frequency peak of higher frequency and amplitude is also generated and can be attributed to the X-shaped wavefront, with a slightly shorter wavelength, shown in the aeroacoustic field. It can be noticed that the frequency features of the combined effects of the flow, source, and cylindrical liners are present in this case, as shown in Figure 3.40. Moreover, some of the harmonics present in the first case have lower amplitude than the broadband frequency content generated by the interaction of the flow with the resonators array and are, consequently, not visible in the response.

Finally, Figure 3.41 presents the SPL spectrum obtained for all of the cases, i.e., the plane channel with flow and source, flow, and the acoustic treatment using the cylindrical liners with and without the harmonic source. When comparing the cases with source only and linear plus source, it can be highlighted that the SPL reduction at the driving frequency is of 5; dB, in the first harmonic, 20; dB, for the second harmonic, 23.5; dB, for third, and 15.5; dB, for the fourth one. However, a significant increase in the overall broadband noise is created, as previously discussed.

In the next Chapter, some concluding remarks are presented along with suggestions for further work.

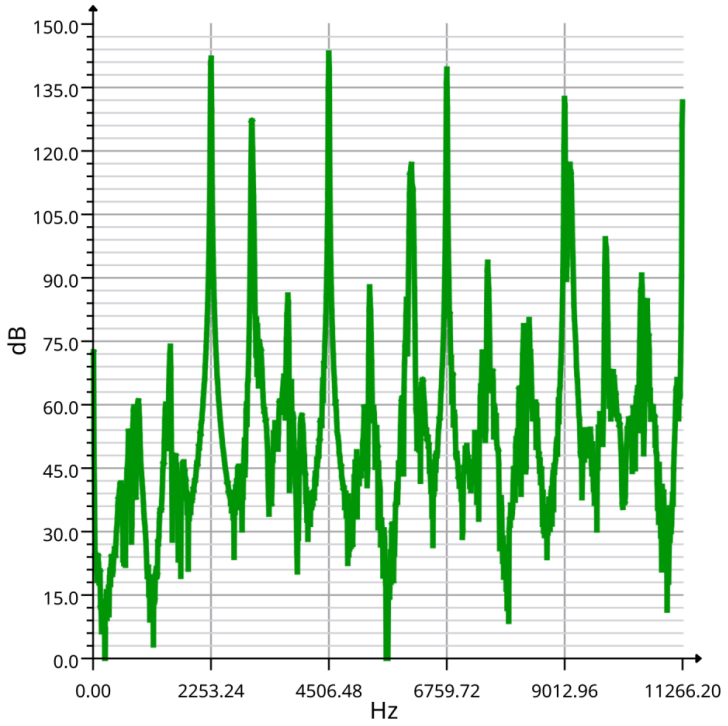

Figure 3.38 – Sound pressure level spectrum at the inlet of the channel for the flow and source case.

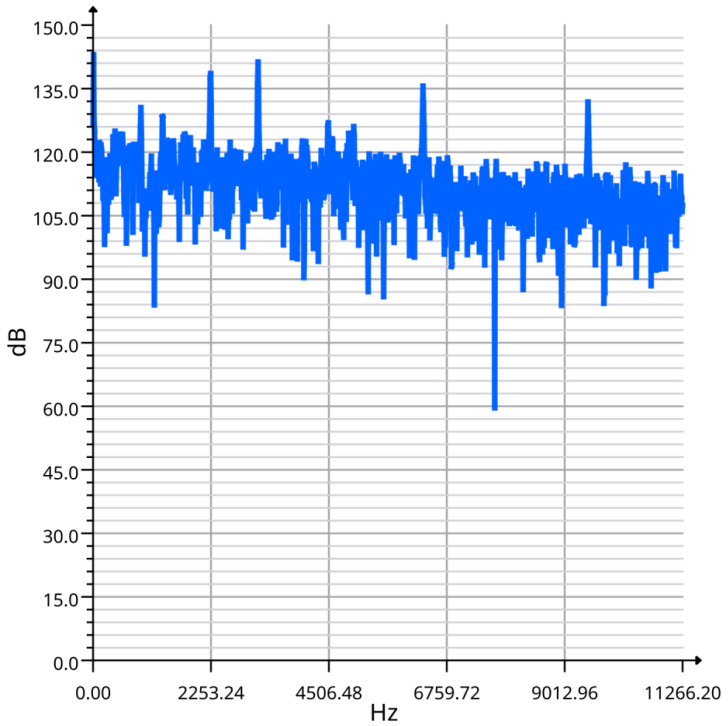

Figure 3.39 – Sound pressure level spectrum at the inlet of the channel for the flow and cylindrical liners case.

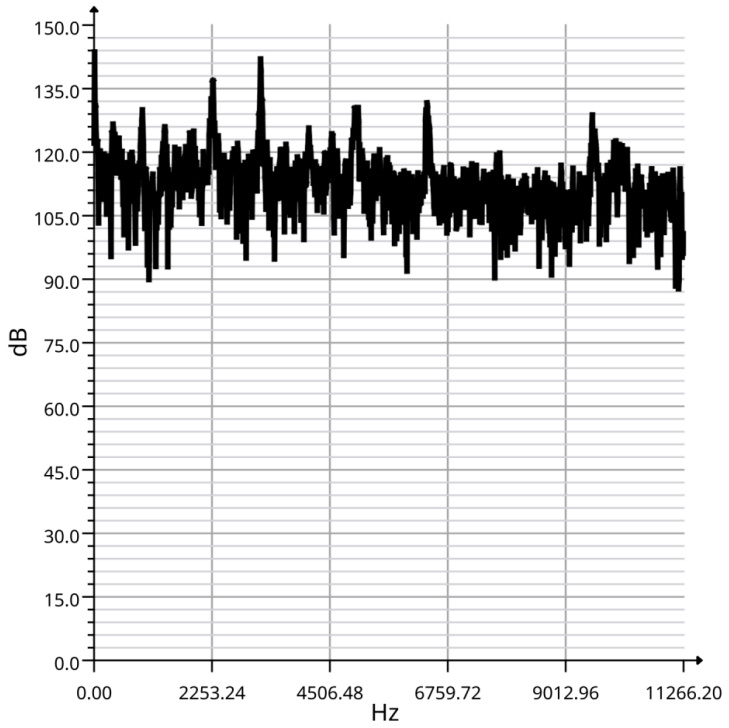

Figure 3.40 – Sound pressure level spectrum at the inlet of the channel for the flow, source, and cylindrical liners case.

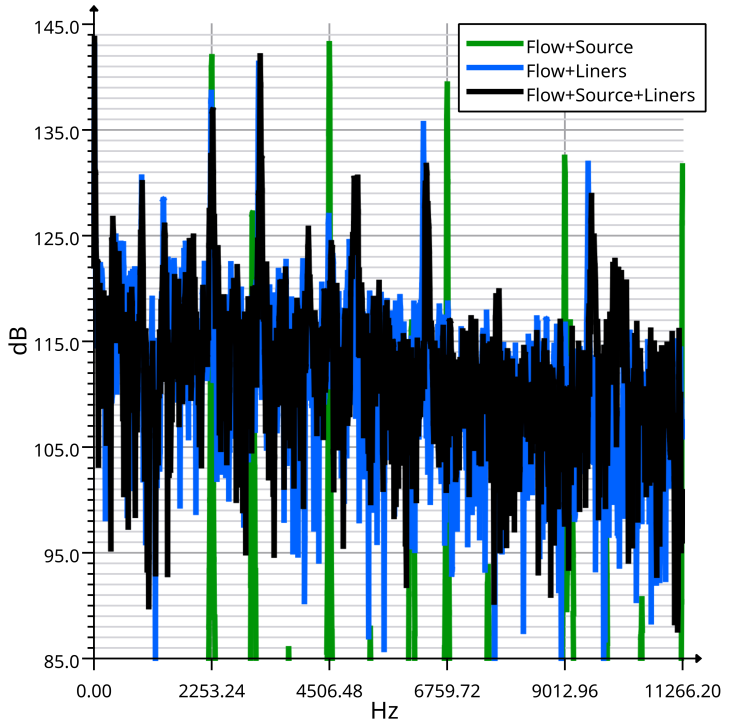

Figure 3.41 – Effect of the acoustic treatment using cylindrical liners on the sound pressure level at the inlet of the channel.

4 Conclusion

In this work, a numerical approach was proposed to investigate the acoustic interaction of a lined array of resonators when subject to high subsonic flow and high amplitude pressure sources. Three test cases are investigated with increasing complexity. In the first, a simple channel with the flow and a nonlinear source shows the potential of the proposed numerical approach for generating plane waves. In the second configuration, a lined channel with subsonic flow shows the generation of nonlinear plane waves with the same frequency and similar pressure levels when compared with the first case. Finally, the two previous configurations are combined, introducing a high-pressure nonlinear source in the lined configuration with a high subsonic flow. The latter is typically found at interstage regions of very high bypass ratio turbofans and counter/corotating rotors for eVTOL applications.

The obtained results show that the numerical methodology was able to simulate the acoustic attenuation of tone noise produced by a nonlinear source in a high subsonic flow when an array of cylindrical liners is used. It is shown that for the first harmonic of the nonlinear source, 2253.24Hz, the tone noise reduction is 5dB, as well as 20dB for the second harmonic, 23.5dB for the third one, and 15.5dB for the fourth. On the other hand, broadband noise content appears due to the cylindrical liners. However, this content is at least 20dB lower than the peak of 144dB associated with the second harmonic of the untreated nonlinear source.

4.1 Suggestions for further work

Further work includes extending this analysis to different geometries, investigating the influence of dimensions, geometry, number of resonators in the array. Moreover, it is also suggested to include a deeper investigation on all of the dynamic features and wave types generated in this configuration as well as of the resulting broadband features of the response due to the interaction of the flow and liners. For this investigation, it is suggested the use of a more systematic approach using modern signal processing approaches for the full aeroacoustic field, such as the Proper Orthogonal Decomposition, or for the time domain results collected in measurement probes across the computational domain, using non-linear time series analysis.

Bibliography

BÖTTCHER, J. *Noise Certification Workshop*: Session 2: Aircraft noise certification. 2004. Disponível em: <https://www.icao.int/Meetings/EnvironmentalWorkshops/Documents/NoiseCertificationWorkshop-2004/BIP_2_2_jb.pdf>. Citado 3 vezes nas páginas xii, 2, and 3.

CFR Title 14: Aeronautics and Space: Part 36 — noise standards: Aircraft type and airworthiness certification. 1969. Disponível em: <https://www.ecfr.gov/cgi-bin/retrieveECFR?gp=&SID=848a71308ceac7a9cc4798db08de4dac&n=14y1.0.1.3.19&r=PART&ty=HTML>. Citado na página 2.

DEAN, P. D. An in situ method of wall acoustic impedance measurement in flow ducts. *Journal of Sound and Vibration*, v. 34, n. 1, p. 97–130, 1974. Citado na página 6.

DEPITRE, A. *Noise Certification Workshop*: Session 2: Epndb metric. 2006. Disponível em: <https://www.icao.int/Meetings/EnvironmentalWorkshops/Documents/Noise-Certification-Workshop-2006/Depitre_4.pdf>. Citado na página 1.

DOWLING, A. P.; HUGHES, I. J. Sound absortion by a screen with a regular array of slits. *Journal of Sound and Vibration*, v. 156, n. 3, p. 387–405, 1992. Citado na página 6.

ELDREDGE, J. D.; DOWLING, A. P. The absorption of axial acoustic waves by a perforated liner with bias flow. *Journal of Fluid Mechanics*, Cambridge University Press, v. 485, p. 307–335, 2003. Citado na página 6.

ENFLO, B. O.; HEDBERG, C. M. *Theory of Nonlinear Acoustics in Fluids*. New York: Kluwer Academic Publishers, 2002. Citado na página 4.

HERSH, A. S. et al. Helmholtz resonator impedance model, part 1: Nonlinear behaviour. *AIAA Journal*, v. 41, n. 5, p. 795–808, 2003. Citado 2 vezes nas páginas 4 and 7.

HUGHES, I. J.; DOWLING, A. P. The absortion of sound by perforated linings. *Journal of Fluid Mechanics*, v. 218, p. 299–335, 1990. Citado na página 6.

ICAO. *The Convention on International Civil Aviation*. 2012. Disponível em: <https://www.icao.int/safety/airnavigation/nationalitymarks/annexes_booklet_en.pdf>. Citado na página 1.

JAMESON, A. et al. Numerical solution of the euler equations by finite volume methods using runge-kutta time stepping schemes. *AIAA Paper*, v. 81, 07 1981. Citado na página 14.

JING, X. et al. Effect of grazing flow on the acoustic impedance of an orifice. *AIAA Journal*, v. 39, p. 1478–1484, 08 2001. Citado na página 7.

JING, X.; SUN, X. Experimental investigations of perforated liners with bias flow. *The Journal of the Acoustical Society of America*, v. 106, n. 5, p. 2436–2441, 1999. Citado na página 6.

MALMARY, C. et al. Acoustic impedance measurement with grazing flow. 05 2001. Citado na página 7.

MELLING, T. H. The acoustic impedance of perforated at medium and high sound pressure levels. *Journal of Sound and Vibration*, v. 29, n. 1, p. 1–65, 1973. Citado na página 6.

MISERDA, R. et al. Numerical simulation of rotor-stator interaction noise in transonic cascades. *Journal of Propulsion and Power*, v. 36, p. 1–18, 03 2020. Citado 2 vezes nas páginas 4 and 17.

MOTSINGER, R. E.; KRAFT, M. E. Design and performance of duct acoustic treatment. In: . [S.l.: s.n.], 1991. Citado na página 5.

ÖZYÖRÜK, Y. et al. Time-domain numerical simulation of a flow-impedance tube. *Journal of Computational Physics*, v. 146, p. 29–57, 1998. Citado na página 7.

PIMENTA, B.; MISERDA, R. Numerical simulation of multiple pure tone noise generated by supersonic rotor cascades. *Journal of Propulsion and Power*, v. 35, p. 1–14, 03 2019. Citado 2 vezes nas páginas 4 and 17.

PIMENTA, B. G. *Numerical Simulation of Nonlinear Waves in Gas Dynamics and Rotor-Stator Interaction Noise of Aeronautic Turbofan Engines*. 2016. 229 p. Tese (Doutorado). Citado na página 13.

SMITH, M. J. T. *Aircraft Noise*. [S.l.]: CAMBRIDGE UNIVERSITY PRESS, 1989. Citado 2 vezes nas páginas 1 and 4.

SPILLERE, A. *Towards optimal design of acoustic liners in turbofan aero-engines*. 06 2017. Tese (Doutorado). Citado 2 vezes nas páginas xii and 6.

SUTLIFF, D. L. Rotating rake turbofan duct mode measurement system. *The Journal of the Acoustical Society of America*, v. 118, n. 3, p. 1864–1864, 2005. Citado na página 4.

TAM, C. et al. A computational and experimental study of slit resonators. *Journal of Sound and Vibration*, v. 284, n. 3, p. 947 – 984, 2005. ISSN 0022-460X. Disponível em: <http://www.sciencedirect.com/science/article/pii/S0022460X04006042>. Citado na página 7.

TAM, C. et al. A numerical and experimental investigation of the dissipation mechanisms of resonant acoustic liners. *Journal of Sound and Vibration*, v. 245, n. 3, p. 545 – 557, 2001. ISSN 0022-460X. Citado na página 7.

TAM, C. et al. Experimental validation of numerical simulations for an acoustic liner in grazing flow: Self-noise and added drag. *Journal of Sound and Vibration*, v. 333, p. 2831–2854, 06 2014. Citado na página 7.

TAM, C. K. et al. Numerical simulation of a slit resonator in a grazing flow under acoustic excitation. *Journal of Sound and Vibration*, v. 313, n. 3, p. 449 – 471, 2008. ISSN 0022-460X. Citado 2 vezes nas páginas 4 and 7.

TAM, C. K. W.; AURIAULT, L. Time-domain impedance boundary conditions for computational aeroacoustics. *AIAA Journal*, v. 34, n. 5, p. 917–923, 1996. Citado na página 7.

TAM, C. K. W.; KURBATSKII, K. A. Microfluid dynamic and acoustic of resonant liners. *AIAA Journal*, v. 38, n. 8, p. 1331–1339, 2000. Citado na página 7.

YEE, H. Explicit and implicit multidimensional compact high-resolution shock-capturing methods:formulation. *Journal of Computational Physics*, v. 131, n. 1, p. 216–232, 1997. ISSN 0021-9991. Disponível em: <https://www.sciencedirect.com/science/article/pii/S0021999196956089>. Citado na página 15.

ZHANG, Q.; BODONY, J. Numerical simulation of two-dimensional acoustic liners with high speed grazing flow. *AIAA Journal*, v. 49, p. 365–382, 02 2011. Citado na página 7.